Remote Sensing of Environment 198 (2017) 407–424

Contents lists available at ScienceDirect

Remote Sensing of Environment

journal homepage: www.elsevier.com/locate/rse

Approaches for synergistically exploiting VIIRS I- and M-Band data in regional active fire detection and FRP assessment: A demonstration with respect to agricultural residue burning in Eastern China

Tianran Zhang [a,b,*], Martin J. Wooster [a,b], Weidong Xu [a,b]

[a] King's College London, Department of Geography, Strand, London WC2R 2LS, United Kingdom
[b] NERC National Centre for Earth Observation (NCEO), United Kingdom

ARTICLE INFO

Article history:
Received 29 October 2016
Received in revised form 9 June 2017
Accepted 25 June 2017
Available online xxxx

Keywords:
FRP
VIIRS
Biomass burning
Agricultural fire
MODIS

ABSTRACT

We demonstrate a new active fire (AF) detection and characterisation approach for use with the VIIRS spaceborne sensor. This includes for the first-time joint exploitation of both 375 m I-Band and 750 m M-Band data to provide both AF detections and FRP (fire radiative power) retrievals over the full range of fire and FRP magnitudes. We demonstrate the value of our VIIRS-IM 'synergy' product in an area of eastern China dominated by numerous small agricultural residue burns, which contribute significantly to regional air quality problems but which are often difficult to identify via standard (e.g. MODIS 500 m resolution) burned area mapping. We show that the highly 'fire sensitive' VIIRS I-Band data enables detection of the 'small' active fires (FRP ≤ 1 MW), but this sensitivity can lead to false alarms, often associated with manmade structures. We help avoid these via use of 30 m resolution global land cover data and an OpenStreetMap mask. Comparisons to near-simultaneous Aqua-MODIS AF detections, and the existing VIIRS I-Band AF global product, highlight our VIIRS algorithm's ability to more reliably detect the lowest FRP pixels, associated with the type of agricultural burning dominating eastern China. Our algorithm delivers typically 5 to 10× more AF pixels than does simultaneous-collected MODIS AF data (notwithstanding differences in spatial resolution), and importantly with a AF detection sensitivity that remains much more constant across the swath due to VIIRS' unique pixel aggregation scheme. The VIIRS I4-Band saturates over higher FRP fires, but by combining use of I- and M-Band data our algorithm generates reliable FRP records for all fires regardless of FRP magnitude. Using the VIIRS-IM methodology we find regionally summed FRP's up to 4× higher than are recorded by MODIS over the same fire season, highlighting the significance of the formally undetected low FRP active fires and indicating that current MODIS FRP-based emissions inventories for areas dominated by agricultural burning may be underestimating in a similar way to burned-area based approaches. FRP generation from VIIRS that takes into account both low- and high-FRP fires via use of both the I- and M-Band data should therefore enable significant improvements in global fire emissions estimation, particularly for regions where smaller types of fire are especially dominant.

1. Introduction

Satellite remote sensing is widely used for mapping burned area (Giglio et al., 2010; Roy et al., 2008) and for detecting and characterising actively burning fires (Giglio et al., 2006, 2008; Roy et al., 2005, 2008; Wooster et al., 2005). Burned area (BA) products generally require a substantial fraction of the pixel to be fire-affected for a confident detection to be made, whereas active fires only need cover 0.01–0.1% of the pixel area (Giglio et al., 2006, 2008; Robinson, 1991; Roberts et al., 2005; Schroeder et al., 2014). Randerson et al. (2012) compared 500 m spatial resolution (MCD64A1) MODIS BA data to 1000 m spatial resolution (MOD14/MYD14) MODIS AF (active fire) data to highlight the fact that a large proportion of the typical 'small' fires found in agricultural and tropical deforestation landscapes appear to remain undetected in the BA data, but do appear in the AF products. Burned area is therefore significantly underestimated in such areas, with the most severe impacts (>50% underestimation) apparently located in parts of central Asia where agricultural residue burning across huge numbers of individually small fires dominates. This estimate of the degree of underestimation is itself very uncertain, and maybe a minimum estimate because the MODIS AF product itself often fails to detect active fires whose FRP is significantly below ~8 MW (Zhukov et al., 2006). This minimum detection threshold becomes even higher away from the MODIS swath centre (Freeborn et al., 2011). In most biomes and for most times of year, such low FRP fires seem likely to dominate (e.g. Wooster and

* Corresponding author.
E-mail address: tianran.zhang@kcl.ac.uk (T. Zhang).

http://dx.doi.org/10.1016/j.rse.2017.06.028

Zhang, 2004; Ichoku et al., 2008), so in addition to their potential use in improving the estimation of burned area, low FRP AF detection may also be very significant for regional fire regime characterisation (Freeborn et al., 2014) and for FRP-based smoke emissions assessments (e.g. Kaiser et al., 2012).

Here we present a new AF detection approach, based on data from the Visible Infrared Imaging Radiometer Suite (VIIRS) carried on the Suomi-NPP satellite. The approach is aimed specifically at including detection and characterisation of low FRP fires as well as the much easier-to-detect high FRP fires. Via this approach, we aim to much more fully record regional FRP characteristics at the time of the satellite overpass than hitherto possible.

VIIRS has two middle-wave infrared (MWIR) bands offering (at nadir) 375 m (I-Band) and 750 m (M-Band) spatial resolutions, representing significantly smaller pixel areas and thus an improved active fire detection capability than offered by MODIS (with its 1000 m spatial resolution nadir pixels). Whilst the experimental Hotspot Recognition Sensor (HSRS) on-board the BIRD satellite has previously been used to demonstrate a low-FRP detection capability based on sub-400 m spatial resolution data (Zhukov and Oertel, 2001; Zhukov et al., 2006), unlike BIRD-HSRS, VIIRS offers global twice daily observations. This includes an overpass in the early afternoon, at around the peak of the usual fire diurnal cycle (Freeborn et al., 2011). We apply our analysis of VIIRS data to detect and quantify active fires burning in the agricultural region of eastern China, which Randerson et al. (2012) demonstrate is an area where omission of 'small' crop residue fires by the MODIS (MCD64A1) BA product appears among the most significant worldwide.

Schroeder et al. (2014) have already demonstrated an improved ability to detect 'small fires' using the VIIRS I-Band. Fires down to an FRP around an order of magnitude lower than the minimum detection limit of MODIS can in theory be detected, due to the I-bands 10× smaller (nadir) pixel area. The resulting VIIRS AF product from Schroeder et al. (2014) (VNP14IMGTDL_NRT) indeed shows a generally much more sensitive 'small fire' active fire detection performance compared to the MODIS MOD14/MYD14 product, though the implementation described in Schroeder et al. (2014) did not include FRP retrieval itself. The generally strong performance of the Schroeder et al. (2014) global-I-Band algorithm has inspired our regional algorithm, in which we combine VIIRS I- and M-Band data to generate AF detections and FRP retrievals for both low- ("small") and high-FRP ("large") fires. We optimise our algorithm for eastern China, an area of agricultural burning where the Schroeder et al. (2014) global implementation still has some difficultly, showing a high rate of low confidence AF detections. We compare outputs from our VIIRS I-M synergy product scheme to those from the global algorithm of Schroeder et al. (2014), and to MODIS, illustrating the impact of our enhancements related to both AF detection and FRP characterisation.

2. The VIIRS sensor, scan and data characteristics

2.1. VIIRS sensor

VIIRS currently operates onboard Suomi-NPP (launched October 2011), and is the first of a set of 22-band scanning radiometers designed to fly on the Joint Polar Satellite System (JPSS) over the coming decades (Wolfe et al., 2013). VIIRS offers one set of multi-spectral channels (five "I-Bands") providing 375 m spatial resolution data (at nadir), and a further set (sixteen "M-Bands") recorded simultaneously at 750 m spatial resolution (at nadir). One M-Band pixel thus contains four I-Band pixels.

Table 1 shows the VIIRS bands used herein, and the two I-Bands bands centred on middle and longwave infrared wavelengths (3.74 and 11.45 μm respectively) make it possible to quite easily adapt existing AF detection algorithms (e.g. Giglio et al., 2003) for use with VIIRS I-Band data. In theory, because the I-Band's pixel areas are 10× smaller than MODIS (at nadir), active fires around 10× smaller in area (or with ~10× lower fire intensity FRP), are detectable with VIIRS compared to MODIS.

2.2. VIIRS scan and data characteristics

In addition to its higher spatial resolution, a key difference between VIIRS and MODIS is the former's 'pixel aggregation' scheme which limits pixel area increase with scan angle to a maximum of ×4 compared to MODIS' × 10 (Wolfe et al., 2013). Via this scheme, the standard ungeocoded VIIRS SDR (Sensor Data Record, equivalent to MODIS Level 1b) data (Fig. 1a) is separated into different aggregation zones, with each pixel in 'Aggregation Zone 3' being the signal average of three along-scan sub-pixels, those in 'Aggregation Zone 2' being the average of two sub-pixels, and those in the 'No Aggregation Zone' being the original observations (Wolfe et al., 2013). This greatly lessens VIIRS pixel area increase across the swath, but the data still suffer a MODIS-like "bow tie effect" towards the swath edge due to overlap between consecutive scans (Wolfe et al., 2013). To counteract this, the VIIRS SDR has the four outermost sampling rows of an individual scan line filled with zeros across Aggregation Zone 2, and eight across the outermost "No Aggregation Zone" (Fig. 1). This removes the "bow-tie" effect seen in ungeocoded MODIS level 1b data, where near swath-edge pixels appear replicated along-track due to their dimensions being far larger than the satellites along-track movement during a single scan (Wolfe et al., 2013).

Schroeder et al. (2014) identified a series of key issues to address prior to confident use of VIIRS data for AF detection and fire characterisation. Of utmost relevance to FRP retrieval is that the I-Band covering the MWIR spectral region (I4) saturates at 367 K, and because of the small ground footprint of the pre-aggregation I-Band detectors - such a brightness temperature can be reached at the locations of even rather low-to-moderate FRP fires (e.g. ~20 MW or less). Unfortunately, the VIIRS data Quality Flag (QF) currently only shows instances where all the pre-aggregation VIIRS pixels going into the signal averaging calculation are saturated, which is a far less common situation than only a subset of them being saturated. Thus, it is a non-straightforward task to unambiguously identify all I4 Band pixels affected by pre-aggregation saturation, and we address this issue via synergistic use of the 750 m MWIR M13 band data at all such potential locations, as explained in Section 6.

3. Study area

Our 1.1 million km^2 eastern China study region includes the North China Plain and the Yangtze Plain (Fig. 2), encompassing around one

Table 1
VIIRS spectral bands used herein, along with the closest bands of MODIS for reference (from Cao et al., 2013).

VIIRS band	Spectral range (μm)	Spatial resolution @ nadir (m)	MODIS band	Spectral range (μm)	Spatial resolution @ nadir (m)
I1	0.600–0.680	375	1	0.620–0.670	250
I2	0.846–0.885	375	2	0.841–0.876	250
I3	1.580–1.640	375	6	1.628–1.652	500
I4	3.550–3.930	375	20	3.660–3.840	1000
I5	10.500–12.400	375	31 or 32	10.780–11.280	1000
				11.770–12.270	1000
M13	3.973–4.128	750	21 or 22	3.929–3.989	1000
				3.929–3.989	1000

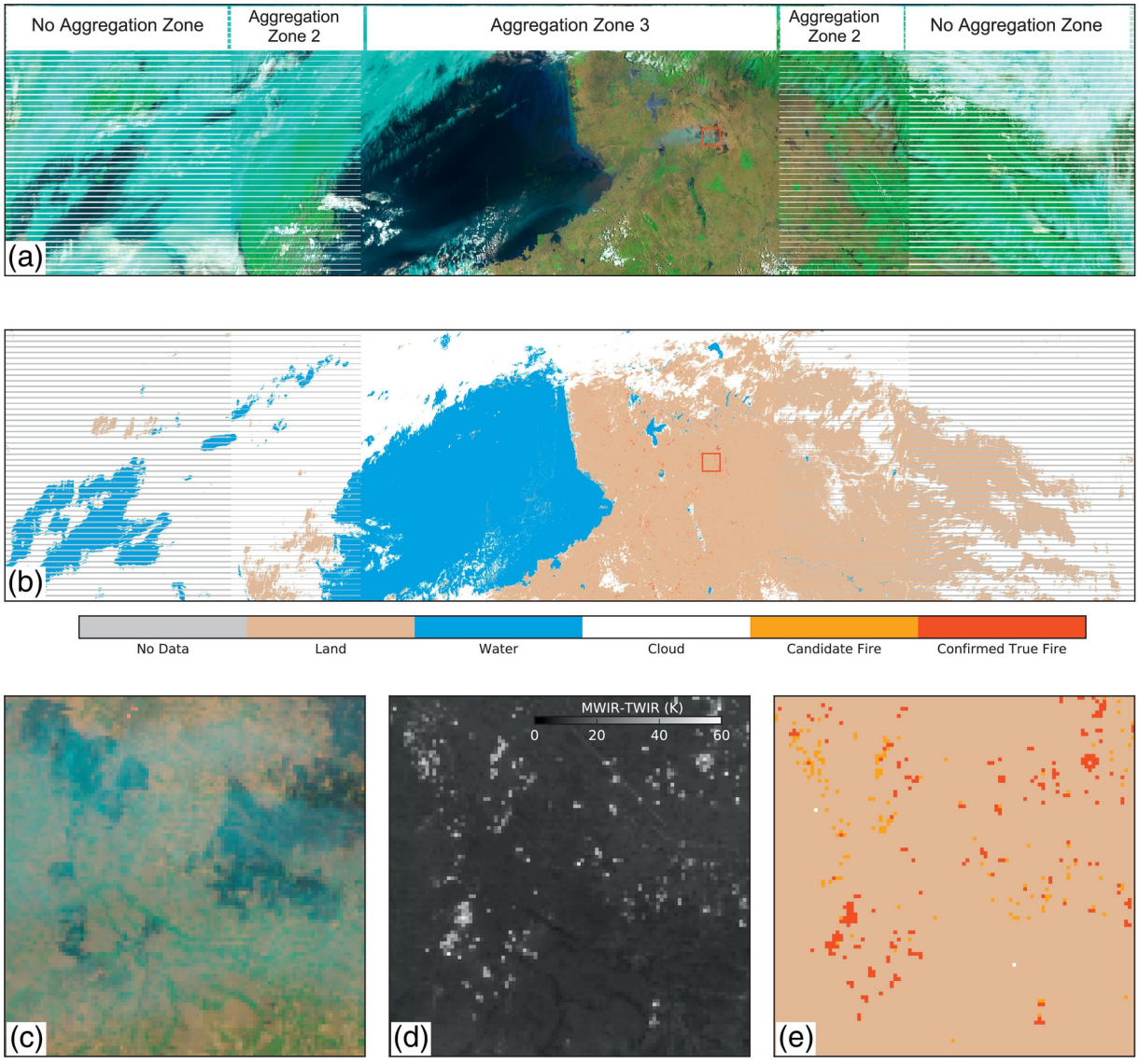

Fig. 1. VIIRS data of eastern China, covering the area outlined in yellow in Fig. 2. (a) VIIRS I-Band false colour composite image (RGB = I3, I2, I1) with the region selected and shown as (c), (d), and (e) outlined in red. (b) cloud/water/candidate thermal anomaly pixel/confirmed thermal anomaly pixel (white/blue/orange/red) derived from I-Band data using the techniques detailed herein. (c) shows the same false colour composite as in (a), but now zoomed on the highlighted region. These data are subset from the first 85-second granule of VIIRS SDR npp_d20150613_t0503225_e0509028. (d) shows the MWIR (Band I4) and LWIR (Band I5) brightness temperature difference image matching (c), and (e) shows the matching cloud/water/candidate fire/confirmed active fire pixel mask output from our active fire detection scheme outlined in Fig. 3. The image is an ascending node scene, with north towards the bottom. (For interpretation of the references to colour in this figure legend, the reader is referred to the web version of this article.)

third of the Chinese population and the area responsible for an estimated 25% of China's crop production (~51% of the national rice yield; NBSC, 2012). Burning typically remains the quickest, simplest and cheapest approach to removing agricultural residues left after harvest of rice, wheat, and other crops, and remains commonplace even though discouraged or forbidden since the late 1990's (Huang et al., 2012). Until recently such crop residues were China's second largest industrial waste product (Qu et al., 2014), and this widespread burning is suspected of contributing significantly to China's air quality problems (Qu et al., 2014). Previous studies show most fields in eastern China support at least two crops per year (Huang et al., 2012; Pan et al., 2013), with winter wheat harvested in June, the stubble burnt shortly after, and the fields then rapidly flooded and rice planted. This rice is harvested in September or October when the fields are also drained, the rice straw burned, and the fields prepared again for wheat planting (Huang et al., 2012).

Being almost solely confined to agricultural fields, the individual crop residue fires themselves may each be quite small, but they occur in extremely large numbers (Huang et al., 2012). Mostly ignited within a few weeks in any particular area (usually twice per year), their cumulative impact on air pollution at these times can seemingly be very high (Huang et al., 2012; Yan et al., 2006). However, whilst 1 km MODIS MOD14/MYD14 AF data indicate their spatial patterns (Fig. 2), and perhaps allow improved quantification compared to MODIS 500 m burned area data alone (which seems to miss large fractions of the activity; e.g. Randerson et al., 2012), the typically small individual size (and thus low FRP) of the fires means that many still remain unaccounted even when using the MODIS AF data (Schroeder et al., 2014). The higher spatial resolution data from VIIRS, which should enable the detection of significantly lower FRP fires, can thus very likely significantly aid their quantification.

4. Active fire detection methodology

4.1. Datasets

We based our algorithm development and testing on VIIRS SDRs covering eastern China between 1st June 2014 and 30th June 2015

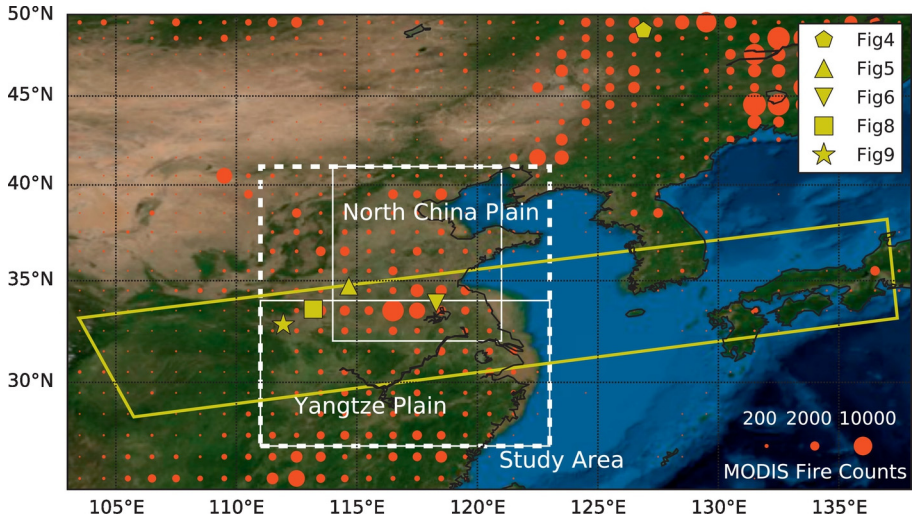

Fig. 2. Eastern China agricultural area (111–123° E, 27–40° N), outlined by the white dashed box. The approximate area of the North China Plain and the Yangtze Plain are demarcated by the solid white boxes. The red circles depict numbers of MODIS active fire pixels detected between 2002 and 2015 per 1° grid cell (see legend lower right). Whilst most fires in the study region are agricultural fires, those towards the north of the wider region include forest fires. Yellow markers show locations of the data of Figs. 4, 5, 6, 8 and 9 (see legend upper right). Yellow outline shows the footprint of the VIIRS swath taken during the 85 s VIIRS SDR used to produce Fig. 1. (For interpretation of the references to colour in this figure legend, the reader is referred to the web version of this article.)

(13 months, covering three burning seasons) and between 12:00 and 15:00 h local solar time by day, and 00:00 to 3:00 by night. An extra VIIRS SDR set for 28th August 2016 was also processed to facilitate comparison of our outputs to the VIIRS global product, which was unavailable for the earlier periods. HDF5 files including all co-registered SDRs were downloaded from NOAA CLASS (https://www.class.ncdc.noaa.gov/), along with the Quality Flag information and common geolocation file. Each 5-min SDR contains four 85-second VIIRS granules (e.g. Fig. 1). For comparison to our VIIRS outputs we used Collection 6 Aqua MODIS MYD14 AF products (Giglio et al., 2016), which closely match VIIRS' overpass time, along with the VNP14IMGTDL_NRT VIIRS I-Band global 'small fire' product based on the algorithm of Schroeder et al. (2014), obtained from https://worldview.earthdata.nasa.gov/ (the Algorithm Theoretical Basis Document and Users' Guide is now available at https://viirsland.gsfc.nasa.gov/Products/FireESDR.html). All data were processed using the UK's JASMIN super-data-cluster (Lawrence et al., 2013).

4.2. VIIRS I-Band regional "small active fire" detection algorithm

Our optimised VIIRS I-Band regional AF detection algorithm has five major steps (Fig. 3), based on a combination of principles taken from the following algorithms: MODIS AF (Giglio et al., 2003, 2016), global VIIRS I-Band (Schroeder et al., 2014), BIRD-HSRS (Wooster et al., 2003; Zhukov and Oertel, 2001; Zhukov et al., 2006), and the Meteosat SEVIRI Fire and Thermal Anomaly (FTA) (Roberts and Wooster, 2008; Wooster

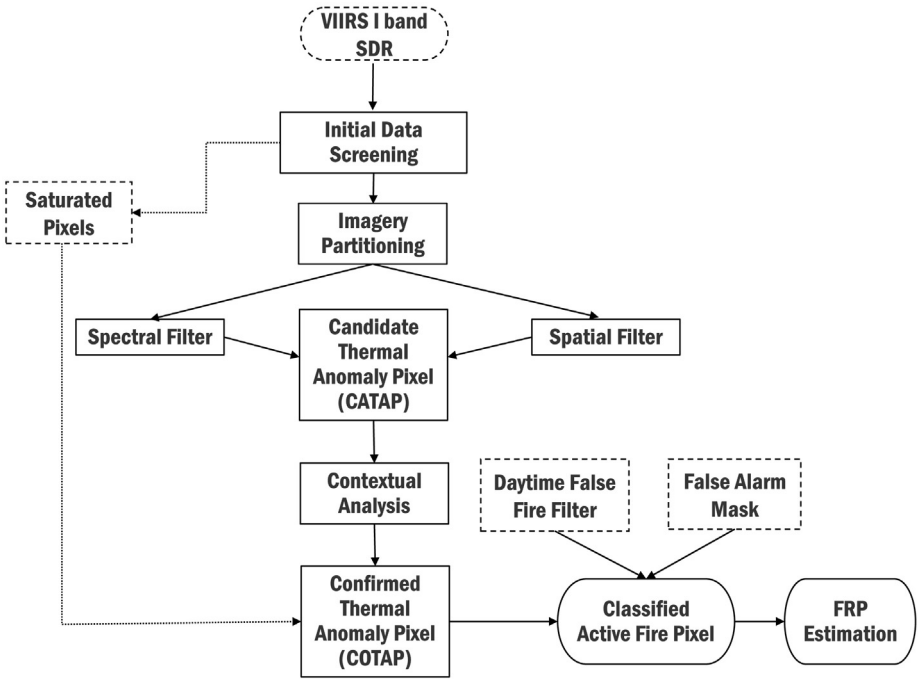

Fig. 3. Workflow of the regionally optimised VIIRS I-Band active fire (AF) detection algorithm developed herein.

et al., 2015). In common with these, our VIIRS algorithm first identifies 'candidate thermal anomaly pixels' whose signals suggest they may possibly contain a fire, and then confirms this via signal comparisons to their surroundings, creating a set of confirmed thermal anomaly pixels. We rely primarily on the VIIRS I4 (MWIR) and I5 (LWIR) spectral channels, with the other three I-Bands used to support cloud/water masking and sunglint discrimination.

Our AF detection algorithm runs at granule level rather than whole VIIRS SDR. In the following description, ρ_i refers to reflectance in VIIRS band i (0 to 1.0), BT_i the brightness temperature (BT) in VIIRS band i (Kelvin), ΔBT_{ij} the BT difference between bands i and j (Kelvin), and QFi the pixel quality flag in VIIRS band i. VIIRS bands are listed in Table 1.

i) Initial data screening

Using its solar zenith angle (θ_s), each VIIRS pixel is classed as day ($\theta_s < 90°$) or night ($\theta_s \geq 90°$), with water and cloud-contaminated pixels removed to reduce computational time in subsequent stages (Schroeder et al., 2014).

For daytime observations, pixels passing six tests taken from Piper and Bahr (2015) are classified as cloud:

$$\rho_1 > 0.08 \quad (1)$$

$$\frac{\rho_1 - \rho_3}{\rho_1 + \rho_3} < 0.7 \text{ AND } \rho_2 > 0.11 \quad (2)$$

$$BT_5 < 300 \text{ K} \quad (3)$$

$$(\max(\rho_3) - \rho_3) \times BT_5 < 410 \text{ K} \quad (4)$$

$$\rho_2/\rho_1 < 2.0 \quad (5)$$

$$\rho_2/\rho_3 > 1.0 \quad (6)$$

where the $\max(\rho_3)$ is the maximum reflectance of VIIRS I3 within the processing scene. The threshold value in (3) is kept at 300 K (cooler than the original implementation) to minimise instances of smoke being classified as cloud.

During night-time passes, a simpler thermal channel cloud threshold is used (Schroeder et al., 2014):

$$BT_4 < 265 \text{ K AND } BT_5 < 295 \text{ K} \quad (7)$$

It is useful to remove water body pixels by day to minimise sunglint impacts, and we use the Schroeder et al. (2014) rapid water mask, with an extra limitation that the I5 BT must lie below 300 K. Without this addition, we found recently burned areas (which are often of low albedo due to their covering of black ash and char) could be incorrectly classed as water, particularly if covered by smoke, as mentioned by Schroeder et al. (2014):

$$\rho_1 > \rho_2 \text{ AND } \rho_2 > \rho_3 \text{ AND } BT_5 < 300 \text{ K} \quad (8)$$

By day, following Schroeder et al. (2014) we also exclude certain radiometrically bright but still fire-free targets, such as sand banks along riverbeds, using:

$$\rho_1 + \rho_2 > 0.6 \text{ AND } BT_5 < 285 \text{ K} \quad (9)$$

AND

$$\rho_3 > 0.3 \text{ AND } \rho_3 > \rho_2 \text{ AND } \rho_2 > 0.25 \text{ AND } BT_4 \leq 335 \text{ K} \quad (10)$$

VIIRS I4 band suffers from saturation over stronger FRP fires, and Schroeder et al. (2014) indicate that complete folding of the digital count (DC) can sometimes occur with recording starting again from a digital count equivalent to 208 K. However, this is far less common than simple saturation is, particularly so over the type of small agricultural fires focused on here. Our algorithm implements the same tests as Schroeder et al. (2014) to identify saturated I4-band pixels:

$$BT_4 = 367 \text{ K AND QF4} = 9 \text{ [both day and night]} \quad (11)$$

AND

$$BT_5 > 290 \text{ K AND QF5} = 0 \text{[daytime] AND } \rho_1 + \rho_2 > 0.7 \text{ [daytime]} \quad (12)$$

Whilst instances of DC "folding" are identified by:

$$\{\Delta BT_{45} < 0 \text{ [both day and night]} \quad (13)$$

AND

$$(BT_5 > 325 \text{ K AND QF5} = 0 \text{ [daytime] OR} \quad (14)$$

$$BT_5 > 310 \text{ K AND QF5} = 0 \text{ [night−time]})\} \quad (15)$$

OR

$$\{BT_4 = 208 \text{ K AND } BT_5 > 335 \text{ K}\} \quad (16)$$

The saturated pixels are excluded from the later contextual analysis tests, but join other confirmed thermal anomaly pixels for step (v) - 'Daytime False Alarm Filter'.

To exclude potential fire affected pixels from inclusion in the background information used in subsequent stages, the pixels most likely to contain fires are identified by:

$$BT_4 > 325 \text{ K AND } \Delta BT_{45} > 20 \text{ K [daytime]} \quad (17)$$

$$BT_4 > 295 \text{ K AND } \Delta BT_{45} > 5 \text{ K [night−time]} \quad (18)$$

ii) Imagery partitioning

This stage excludes 'bowtie deleted' pixels (i.e. the stripes seen in Fig. 1a) from inclusion in the later contextual analysis background windows, ensuring that enough pixels always exist to calculate the background-window statistics no matter where the candidate potential AF pixel lies within the swath. Each granule is partitioned into six sections (the three different aggregation zones either side of nadir shown in Fig. 1a), and in the outermost two sections either side of nadir, 'bowtie deleted' pixels are removed and six new sub-granules constructed. The dimensions of the 'No aggregation Zone' and 'Aggregation Zone 2' are thus changed from 1280 × 1536 and 736 × 1536 pixels to 1280 × 1152 and, 736 × 1344 pixels respectively via this process.

iii) Candidate thermal anomaly pixel (CATAP) identification

This stage selects the candidate pixels to go through the computationally demanding contextual analysis stage. Whilst the low thresholds set in the early algorithm tests enable the maximum number of potential pixels to be included in this set, to avoid unnecessary computational time it is also desirable to remove those extremely unlikely to contain fires. This trade-off is conducted using a combination of spectral and spatial filtering of each sub-image.

To enable maximum sensitivity to low FRP fires, the spectral filter thresholds are based on statistics calculated from blocks of 50 × 50 pixels within each sub-granule (Wooster et al., 2012). The mix of dynamically-adjusted tests, along with fixed thresholding, has also been used in the SLSTR, VIIRS and MODIS Collection 6 AF detection algorithms

(Wooster et al., 2012; Giglio et al., 2016; Schroeder et al., 2014). Within each block (b), the mean brightness temperature of BT_4 and the difference of BT_4 and BT_5 brightness temperature signals ($\overline{BT}_{4b}$ and $\Delta\overline{BT}_{45b}$) are used, and each pixel tested against these to identify it as a candidate thermal anomaly pixel CATAP. For blocks with ≤1% clear land pixels, the fixed threshold of Schroeder et al. (2014) was used but lowered to enable the detection of lower FRP active fires:

$$(BT4>\overline{BT}_{4b}\ \text{OR}\ 320\ \text{K})\ \text{AND}\ (\Delta BT45>\Delta\overline{BT}_{45b}\ \text{OR}\ 10\ \text{K})\ [\text{daytime}] \quad (19)$$

OR

$$(BT4>\overline{BT}_{4b}\ \text{OR}\ 290\ \text{K})\ \text{AND}\ (\Delta BT45>\Delta\overline{BT}_{45b}\ \text{OR}\ 5\ \text{K})\ [\text{night-time}] \quad (20)$$

Roberts and Wooster (2008) introduced use of a spatial high pass (HP) filter to reduce numbers of candidate thermal anomaly pixels unnecessarily selected from larger areas of solar-heated bare ground or other warmed surfaces, reducing computational cost and false alarms. We use a kernel filters (δ_{filter}), growing from size 3 × 3 to 25 × 25 pixels, and locations with filter output exceeding (P) from any kernel filter is retrained.

$$P = HP_{filter} \geq DT \times \delta_{filter} \quad (21)$$

where DT is a function of the solar zenith angle (θ_s):

$$DT = 2.5 - 0.012 \times \theta_s \quad (22)$$

As with the FTA algorithm of Wooster et al. (2015), pixels passing both the spectral and spatial contextual filters are included in the final candidate thermal anomaly pixel set.

iv) Contextual analysis

The contextual analysis stage tests each candidate thermal anomaly pixel against its own background pixel set, in order to confirm whether its signal is sufficiently elevated for it to be considered a confirmed thermal anomaly pixel (COTAP). Background windows sizes extend from 11 × 11 pixels up to a maximum of 31 × 31, until at least 25% of them are considered valid for inclusion and are not themselves cloud covered, water bodies, potential fire pixels or bad quality data. The mean BT of I4 ($\overline{BT}_{4w}$) and I5 ($\overline{BT}_{5w}$), the mean BT difference ($\Delta\overline{BT}_{45w}$) and corresponding standard deviations ($\delta_{4w}, \delta_{5w}, \delta_{45w}$) are then calculated for the selected background window. The absolute I4 and I5 spectral threshold test of Schroeder et al. (2014) have been removed in our regional algorithm, in order to avoid excluding the smallest (lowest FRP) active fires.

Using its background window statistics, a CATAP is confirmed as a COTAP when it meets the criteria below:

Daytime:

$$\Delta BT_{45} > \Delta\overline{BT}_{45w} + 2^{*}\delta_{45w} \quad (23)$$

$$BT_4 > \overline{BT}_{4w} + 3.5^{*}\delta_{4w} \quad (24)$$

$$BT_5 > \overline{BT}_{5w} + \delta_{5w} - 4\ \text{OR}\ \delta'_4 > 5 \quad (25)$$

where δ'_4 refers to the standard deviation of I4 BT of potential fire affected pixels within background window identified using function (17)–(18).

The daytime complementary contextual test from Schroeder et al. (2014), designed to avoid false alarms at desert boundaries is also applied:

$$\rho 2 > 0.15\ \text{AND}\ \overline{BT'_4} < 345\ \text{AND}\ \delta'_4 < 3\ \text{AND}\ BT_4 > \overline{BT'_4} + 6 \times \delta'_4\ [\text{daytime}] \quad (26)$$

where $\overline{BT'_4}$ refers to the average temperature of potential background fires.

A first sun glint rejection test (taken from Roberts and Wooster, 2008), is used to remove any sun-glint induced false alarms, where L4 and L1 refer to the spectral radiance of I-Bands 4 and 1.

$$L4/L1 < 0.018\ \text{for cloud pixels exist within nearby 15 pixels}\ (31 \times 31\ \text{windows}), \quad (27)$$

OR

$$L4/L1 < 0.01\ \text{for cloud pixels not exist within}\ 31 \times 31\ \text{windows}. \quad (28)$$

For the night-time pixels, the criteria for a COTAP changes to:

$$\Delta BT_{45} > \Delta\overline{BT}_{45w} + 3 \times \delta_{45w} \quad (29)$$

$$BT_4 > \overline{BT}_{4w} + 3 \times \delta_{4w} \quad (30)$$

The CATAPs passing all the contextual tests outlined above are set as COTAPs, and passed to the next stage.

v) Daytime false alarm filter

It is possible that the COTAP set contains sunglint-related false alarms, so pixels satisfying the following condition are removed (Schroeder et al., 2014):

$$\theta_g < 15^{\circ}\ \text{AND}\ \rho_1 + \rho_2 > 0.35 \quad (31)$$

OR

$$\theta_g < 25^{\circ}\ \text{AND}\ \rho_1 + \rho_2 > 0.4 \quad (32)$$

where θ_g is the 'glint angle' calculated from:

$$\cos\theta_g = \cos\theta_v \cos\theta_s - \sin\theta_v \sin\theta_s \cos\Phi \quad (33)$$

where θ_g and θ_s are the view zenith and solar zenith angles respectively, and ϕ is the relative azimuth angle (Giglio et al., 2003).

4.3. Cloud mask performance

An appropriate cloud mask is critical for accurate active fire detection (Giglio et al., 2003). As shown in Fig. 1b, our adaptation of Piper and Bahr (2015) successfully identifies pixels with clear cloud-contamination, including over land on the right hand scene edge and over the ocean on the left. Our approach also avoids masking smoke-contaminated pixels in the middle of the land (Fig. 1b–c), where quite a few candidate AF pixels are detected that are most likely real as they accompany large burned areas (Fig. 1c). Fig. 1 also shows that our daytime water mask successfully identifies water bodies, but does not incorrectly mask burned area as water – which was a potential problem identified by Schroeder et al. (2014).

5. Active fire detection output and evaluation

Fig. 4 presents example output from our final, regionally optimised, 'small' active fire detection algorithm (notice these are COTAPs which pass the daytime false alarm filter). In this case, our algorithm identifies almost all (96%) of the AF pixels identified by the global I-Band algorithm of Schroeder et al. (2014), but also a further set of additional detections (15% more). Some clear smoke plumes are associated with the AF pixels detected by both algorithms, but in the imagery alone it is difficult to confidently identify whether our additional detections represent actual active fire locations or not. We therefore employed field validation to gain further understanding and confidence in the AF detection results.

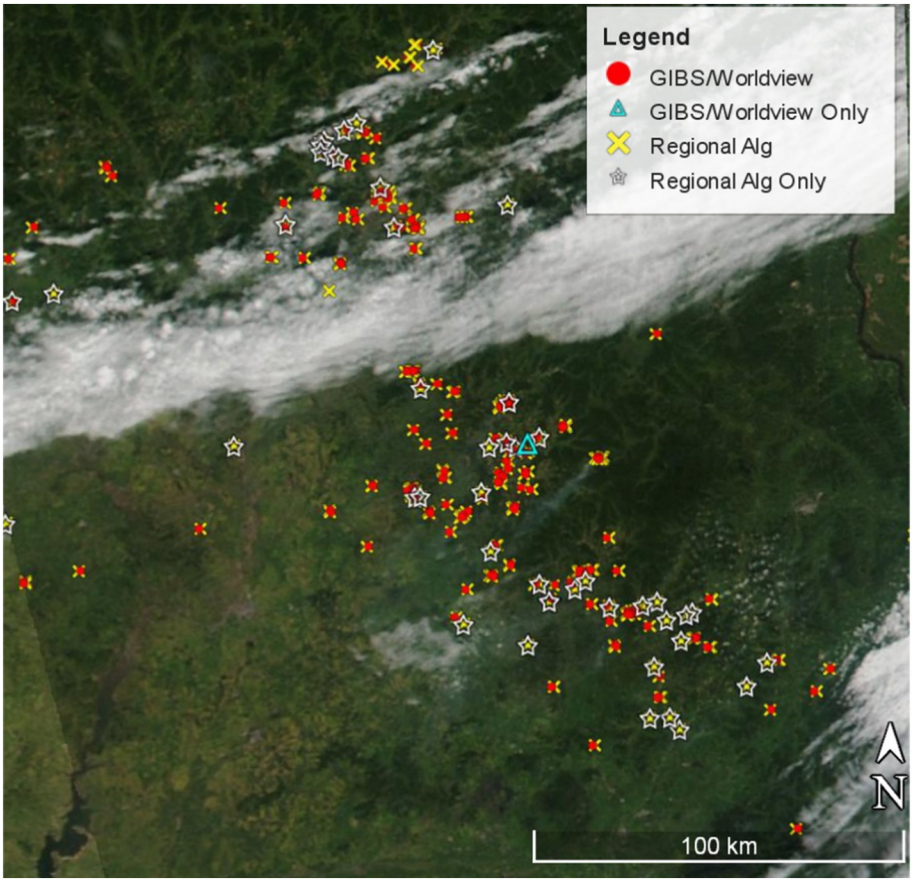

Fig. 4. Active fire pixel detections made on 28 August 2016 from VIIRS, with the scene centre 48.99°N, 126.89°E and a VIIRS true colour composite is used as the basemap. Yellow crosses indicate those AF pixels generated using the regionally optimised VIIRS I-Band AF detection algorithm developed herein, whilst red circles are those output from the global I-Band algorithm of Schroeder et al. (2014) (available from the GIBS/Worldview database). White stars indicate which AF pixel detections were identified only by our regionally optimised I-Band algorithm, and not by the Schroeder et al. (2014) global algorithm. Light blue triangles indicated AF pixels only detected by the global algorithm of Schroeder et al. (2014). (For interpretation of the references to colour in this figure legend, the reader is referred to the web version of this article.)

5.1. Field validation

Field validation (October 2015) involved deploying a small UAV within a few days of a VIIRS confirmed thermal anomaly pixel (COTAP) detection, in order to check for evidence of burning. Thirty COTAPs were examined in total in the Northern China Plain, and for each one recent char and ash were identified clearly in the UAV imagery. Fig. 5 shows one example, where Google Earth Imagery of an agricultural area (34.73° N 114.67° E) taken on 1st October 2015 is shown (Fig. 5a), along with the same scene but with orthomosaiced and geolocated UAV imagery collected six days later overlain (Fig. 5b). Red circles denote the VIIRS I-Band pixel centres which our AF detection algorithm identified as containing fires burning on 5th Oct 2015, and which match recently burned locations in the UAV imagery. Fig. 5d shows more detail, with three different burning patterns seen in the UAV imagery. The large fields on the left show a rather homogeneous covering of black ash and char, indicating a fire that traversed the whole field to burn away crop residues and roots left in the ground (wheat stubble left after harvest is often burned like this). Other fields show a sometimes semi-linear pattern of ash and char, indicating areas where farmers likely gathered up crop residues and burned them in long piles. The rightmost field shows more scattered areas of ash and char, interspersed with apparently unburned areas, indicating perhaps that the farmers had only burned crop roots here. The very patchy and generally quite small nature of the fire-affected areas highlights the great difficulty in mapping burned areas in such agricultural regions, particularly when using relatively coarse spatial resolution imagery of the type provided by MODIS, as pointed out by Randerson et al. (2012).

5.2. False alarm filtering

Schroeder et al. (2014) reported that in eastern China, the global VIIRS I-Band 'small fire' AF detection algorithm shows a high rate of low confidence daytime AF pixels (~40%). This is among the highest proportion seen worldwide, and analysis has shown that many of these low confidence AF pixel detections are in fact false alarms associated with large industrial buildings, having highly reflective and/or warm rooftops and surrounded by more rural landscapes (Fig. 6). Hence, for our regionally optimised algorithm we developed landcover- and hotspot persistence-based spatial filters to identify and remove such occurrences from our algorithm output.

Our landcover-based filter was derived from a combination of 30 m spatial resolution GlobeLand30 global landcover mapping (having an 80% classification accuracy and is derived from 2009 to 2011 Landsat and Chinese land monitoring satellite imagery (http://glc30.tianditu.com/; Chen et al., 2015) and OpenStreetMap (http://www.openstreetmap.org/) data derived from manual surveys, GPS devices, aerial photography, and other free data sources, with layers that include 'places', 'buildings', 'landuse' and 'roads' used here to identify urban areas. We combined GlobeLand30 and OpenStreetMap to generate a binary landcover mask for eastern China at a 0.005° spatial resolution, approximating that of the VIIRS I-Band (Fig. 7a). Cells having a GlobeLand30 crop landcover class cover of ≤40%, or in which any of the four OpenStreetMap 'urban' layers were tagged as 'true', were used to create a spatial mask within which no classified AF pixel detection was allowed to occur. In addition, we also masked as false alarms the thermal anomaly pixels persistently (and unrealistically) detected

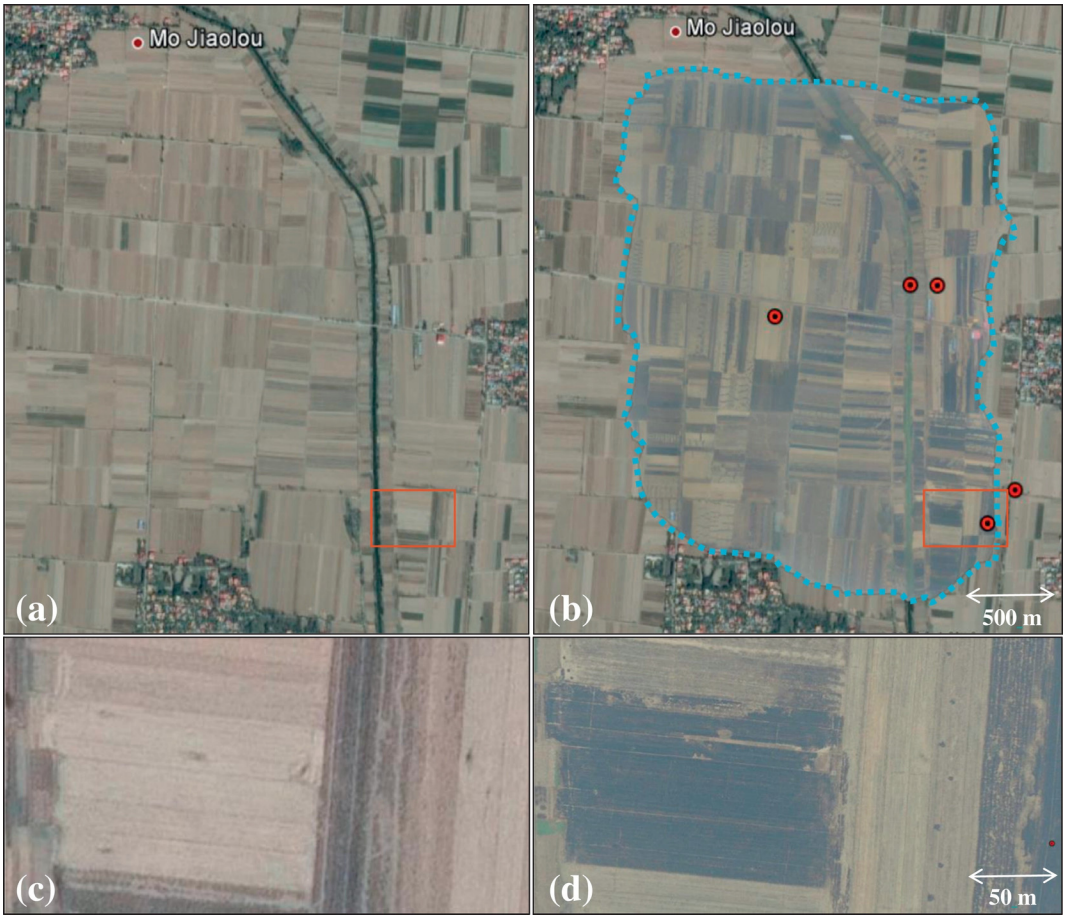

Fig. 5. Validation example taken in Eastern China (34.73° N, 114.67° E). (a) Google Earth imagery dated 1 Oct 2015, with base imagery supplied by CNES/Astrium. (b) mosaiced and geocorrected imagery from our UAV flight (outlined by blue dashed curve) conducted over the area shown in (a) on 7 Oct 2015, one week later than the Google Earth imagery, and with red circles superimposed to show the pixel centres of VIIRS I-Band pixels which our regionally optimised VIIRS I-Band AF detection algorithm detected COTAPs on the afternoon of 5 October 2015. (c) Magnification of the pre-burn area highlighted in (a). (d) Magnification of the post-burn area highlighted in (b), which is the location of a COTAP seen in (a). (For interpretation of the references to colour in this figure legend, the reader is referred to the web version of this article.)

as multiple times in the same locations, and found these again were mostly related to the type of industrial buildings shown in Fig. 6. For this we used a 0.001° spatial resolution mask based on locations where I-Band AF detections were made outside of the burning season four or more times in a single year (Fig. 7b). Fig. 7c illustrates this temporal masks spatial detail for a mixed landuse area, where the mask seems to match up quite well to either urban areas/water bodies (which are assumed to be the sites of repeated false alarms). COTAPs that pass both the spatial and temporal filters are finally classed as AF pixels, and are those used for further analysis and discussion in this study.

Fig. 8 shows an example where confirmed thermal anomaly pixels (COTAPs) identified as 'false alarms' using the masks of Fig.7 are shown in red, and these classified as AF pixels (i.e. that lie outside the masked areas) are in yellow. Classified in this way are both the output from our regional VIIRS I-Band algorithm (smaller polygons reflecting the size of the I-Band pixels), and those generated on the same day and at almost the same time from the MODIS Collection 6 MYD14 product (Giglio et al., 2016). Towards the bottom left of the scene, two clusters of thermal anomaly pixels are detected by both VIIRS and MODIS (along with several more spatially isolated pixels detected only by VIIRS) and each are classified as AF pixels since they are in an agriculturally-dominated area, not one identified as being the location of repeated false alarm detections based on our masking scheme. To the right of the scene centre there are three thermal anomaly pixels initially detected by VIIRS, but classified as confirmed false alarms via our masking and thus not included in the final output AF pixel set. These are all associated with more urbanised landcovers, and whilst not in urban centres they are located at the edges and/or in the suburbs and contain buildings similar to those of Fig. 6. Our procedures correctly remove such thermal anomaly pixels from the final active fire pixel set.

5.3. Comparison to MODIS Aqua active fire detections

Our VIIRS to MODIS AF comparisons were expanded to cover a larger area of eastern China (Fig. 9; 12th June 2015). Here we show the VIIRS I-Band AF detections superimposed on the coarser spatial resolution M-Band imagery. Classified AF pixel locations are indicated by crosses, coloured by FRP (discussed later in Section 6.3). Our VIIRS scheme detects 76 classified AF I-Band pixels, matching to 55 larger M-Band pixels. Far fewer AF pixels (19 in total) are detected by MODIS, and whilst a single MODIS AF pixel may cover multiple I-Band AF pixels, it seems very unlikely that this is the sole cause of the far greater number of VIIRS I-Band AF pixels detections. Rather, the ~10× smaller I-Band pixel area is enabling our algorithm to detect the lower FRP fire pixels that often remain undetected by MODIS, such as in those circled in Fig. 9a.

For the study region of Figs. 2, 10 shows the full 1st June 2014 to 30st June 2015 time-series of classified AF pixel counts made from the VIIRS I-Band (top), along with the AF pixels recorded by MODIS-Aqua (bottom) (day and night-time overpasses). Three burning seasons are covered (June 2014, October 2014 and June 2015), with daytime maxima of ~4000, ~ 2000 and ~3000 AF pixel counts respectively from our VIIRS I-Band scheme and ~700, ~ 500 and ~400 from MODIS. Night-time data show a clear AF peak only in the June burning seasons, with

Fig. 6. Google Earth imagery (33.873° N, 118.294°E) showing the footprints of five false alarm pixels recognized by our I-Band active fire detection algorithm from VIIRS SDR 20140605_t0458444_e0504248 (red polygons with yellow push pins at centre) over large industrial buildings surrounded by a mixture of agricultural lands and rural residential areas. Our false alarm masking approach successfully removes such false detections. (For interpretation of the references to colour in this figure legend, the reader is referred to the web version of this article.)

maxima of ~5000 and ~2000 I-Band AF counts, but only ~140 and ~30 MODIS AF counts. Night-time VIIRS I-Band data of October do still show ~500 AF pixel counts per day, whilst MODIS shows almost none. Overall, our VIIRS I-Band scheme often identifies 5× to 10× more daily AF pixel counts than does MODIS.

6. Fire radiative power (FRP) assessment from VIIRS

Beyond AF pixel detection, fire emissions calculations generally require quantification of the fires radiative power (FRP) output (Wooster et al., 2003, 2005). To minimise impacts from VIIRS I-Band pre-aggregation detector saturation discussed in Section 2.2, we developed an FRP-retrieval scheme to estimate FRP synergistically using both the I-Band and M-Band data.

6.1. FRP estimation

FRP is calculated using the MIR radiance method of Wooster et al. (2003, 2005):

$$FRP = \frac{A}{10^6 \cdot \tau_{MIR}} \frac{\sigma}{a} \left(L_f - \overline{L_b}\right) [MW] \quad (34)$$

where A is the pixel size in m^2, σ is the Stefan–Boltzmann constant (5.67×10^{-8} W m^{-2} K^{-4}), L_f is the VIIRS I4 spectral radiance of the fire pixel (W m^{-2} sr^{-1} μm^{-1}) and $\overline{L_b}$ is the mean background radiance (of the background window), a (3.2146×10^{-9} W m^{-2} sr^{-1} μm^{-1} K^{-4}) is the FRP constant taken from the power-law linking I4 band spectral radiance to the 4th power of emitter temperature (determined using the approach in Wooster et al., 2005), and τ_{MIR} is the VIIRS I4 band atmospheric transmission calculated using the MODTRAN-5 radiative transfer code, standard atmospheric trace gas profiles, and space/time-variable ECMWF total column water vapour and temperature values (http://apps.ecmwf.int/datasets/) as in Wooster et al. (2015).

FRP is estimated for every classified I-Band AF pixel, but because the VIIRS pixel aggregation scheme detailed in Section 2.2 may result in ambiguous I-Band saturation effects, it was also estimated using the M13-Band signal at M-Band pixels within which an I-Band AF detection was made. Due to the 4× larger M-Band pixel area, and greatly increased dynamic range of this channel, only a very few M13 pixel are found to be affected by saturation over active fires (Polivka et al., 2015), and we found none in our study area where the fires are generally relatively small and of low intensity, albeit some can certainly saturate the I4 band.

For the M-band FRP calculation, L_f in Eq. (34) simply uses the M13 spectral radiance, and L_b then becomes that of the M13 band background window, which was allowed to grow from a minimum of 5 × 5 up to 17 × 17 pixels until at least 8 pixels or 1/4 of the window pixels were considered valid for inclusion in the background window set (assessed with a valid M-Band pixel being one where all four constituent I-Band pixels were considered valid via their I-Band classification). The FRP constant a (2.8667×10^{-9} W m^{-2} sr^{-1} μm^{-1} K^{-4}) was calculated as 10.6% lower for M13 than for I4, whilst τ_{MIR} was typically 15% lower for M13 compared to I4 for the same atmospheric profile.

Per-pixel FRP uncertainty (σ_{FRP}; MW) was calculated using standard error propagation as in Wooster et al. (2015):

$$\sigma_{FRP} = FRP \left[\left(\frac{\propto_a}{a}\right)^2 + \left(\frac{\propto_{\tau_{MIR}}}{\tau_{MIR}}\right)^2 + \left(\frac{\propto_{L_b}}{L_f - L_b}\right)^2 + \left(\frac{\propto_{L_f}}{L_f - L_b}\right)^2 \right]^{1/2} \quad (35)$$

This combines the absolute uncertainties ($\propto_a$, $\propto_{\tau_{MIR}}$, $\propto_{L_f}$ and $\propto_{L_b}$) present in the values of the four terms (a, τ_{MIR}, L_f and L_b) of Eq. (35). ($\propto_a/a$) is

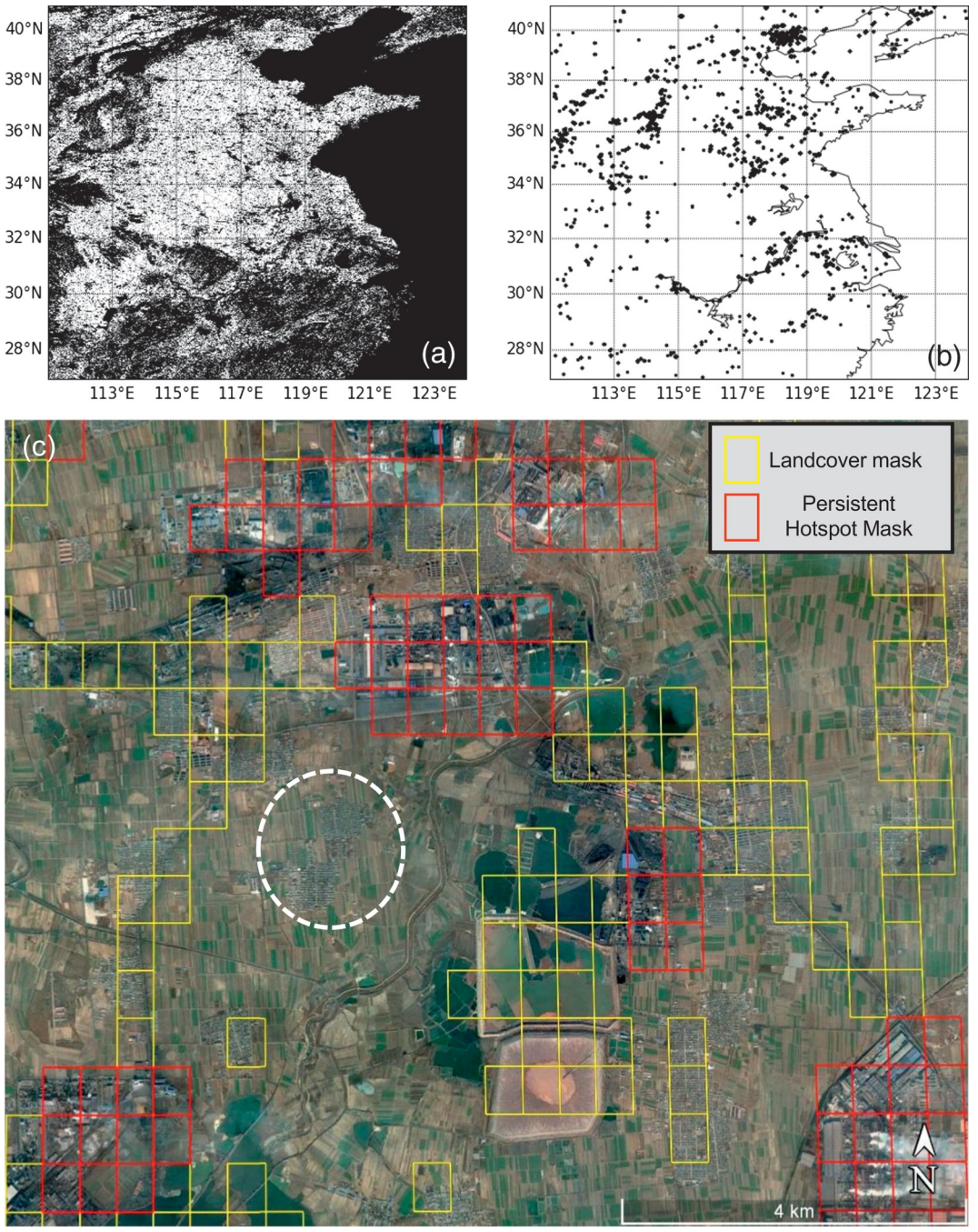

Fig. 7. False alarm mask derived from (a) a binary landcover mask (black pixels) created for eastern China at 0.005° resolution using the GlobeLand30 and OpenStreetMap datasets discussed in the main text, and (b) a map of persistent confirmed thermal anomaly pixel (COTAP) detections, where black pixels indicate locations having four or more COTAP detections in the July 2014 to Sept 2014 and Nov 2014 to May 2015 periods (i.e. outside of the June and October burning seasons), caused by undetected sunglints and industrial heat sources. (c) Google Earth background image (39.588° N, 118.420° E) with locations of mask pixels from (a) and (b) overlain in yellow and red respectively. The white circle outlines an area of urban landuse not included in the current mask, indicating that imperfections still exist in the landcover data and thus that higher quality ancillary data will benefit the algorithm in future. (For interpretation of the references to colour in this figure legend, the reader is referred to the web version of this article.)

equivalent to a 10% uncertainty across the fire temperature range of 650–1350 K (Wooster et al., 2015). $\propto_{\tau_{MIR}}$ contains contributions from both the uncertainty on the actual total atmospheric vertical composition (apart from water vapour), and the water vapour concentration itself (Wooster et al., 2015) (full equations are listed in Appendix A; Eqs. (A1)–(A4)). The absolute uncertainty in the background radiance ($\propto_{L_b}$) is set to the standard deviation of the background window signal in the MWIR band, and the absolute uncertainty in the fire pixel radiance ($\propto_{L_f}$) is set to the sensors radiometric noise in the MWIR channel (0.05 for the VIIRS I4 and 0.007 for M13; Oudrari et al., 2016).

6.2. Comparison of VIIRS and MODIS FRP frequency distributions

Fig. 11 shows the FRP frequency distribution for the study region (June 2014 to June 2015) as calculated from (a, b) the VIIRS I-Band classified AF pixel set, (c, d) the matching VIIRS M-Band data, and (e, f) the corresponding MODIS products (Giglio et al., 2016), which now also use

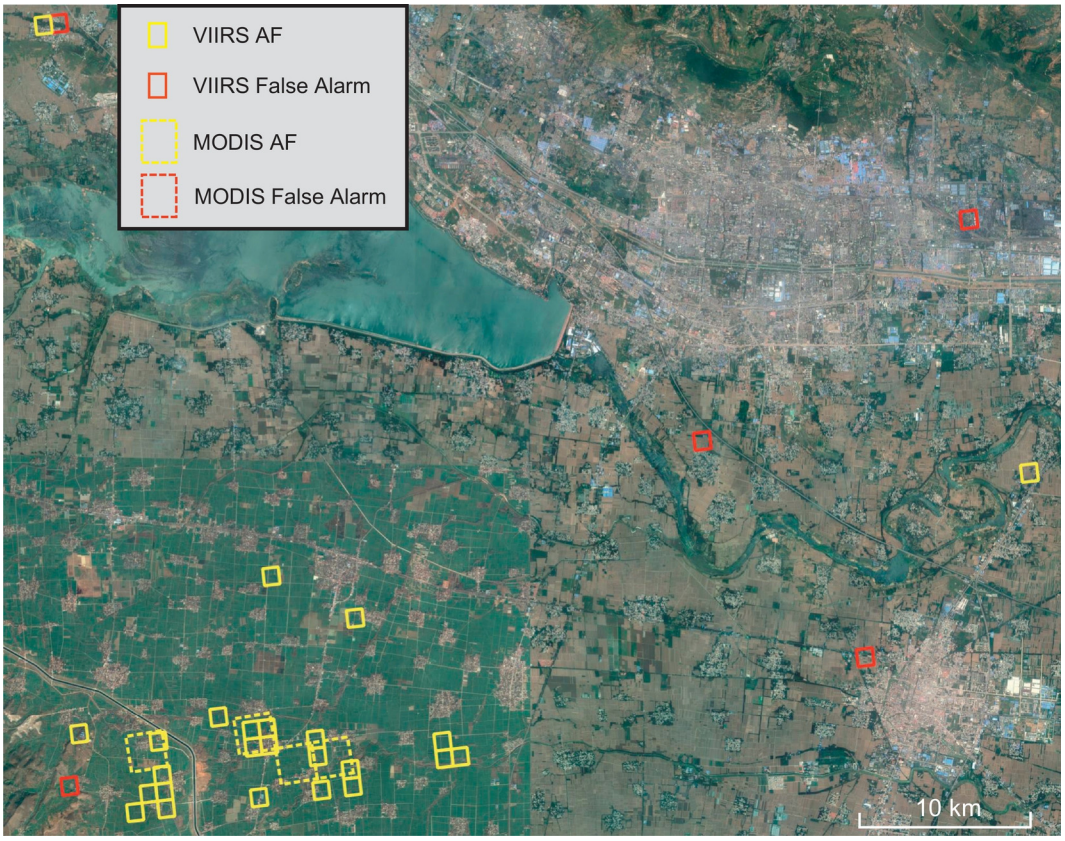

Fig. 8. Locations of confirmed thermal anomaly pixel detections made by our VIIRS I-Band scheme (small polygons) and by MODIS Collection 6 (large dashed polygons). Those classified as false alarms on the basis of the masks shown in Fig. 7 are coloured red, whereas those confirmed as AF pixels are yellow. VIIRS granule is from SDR 20150610_t0555514_e0601318, along with MODIS AF detections from granule A2015161.0545 and a background image from Google Earth. (For interpretation of the references to colour in this figure legend, the reader is referred to the web version of this article.)

Eq. (34) developed by Wooster et al. (2003, 2005) to generate their FRP estimates. We atmospherically corrected the MODIS FRP values using the same MODTRAN-5 based scheme as used with VIIRS.

Data of Fig. 11 approximate a log-normal distribution, being dominated by lower FRP AF pixels and with a long tail of higher FRP AF pixels. For MODIS, the mode (i.e. frequency histogram peak) of the daytime/night-time FRP distributions is 11.8 MW and 7.7 MW respectively, whilst those for VIIRS I-Band are 4.7 MW and 1.5 MW respectively, and for the M-Band 6.3 MW and 2.5 MW respectively. It is important to state that from the M-Band data alone it would often not be generally possible to conclusively detect an AF pixel with an FRP of 2 or 3 MW, as it would raise the 750 m pixels MWIR brightness temperature by only a few Kelvin above background. However, here we are using the I-Band 375 m AF detections to identify the M-Band pixels within which there are actively burning fires, and only using the M-Band data to calculate their FRP and its uncertainty.

Fig. 11 clearly highlights our regional algorithms sensitivity to low FRP fires. However, the VIIRS I-Band observations produce almost no FRP exceeding 30 MW, whereas those from MODIS often extend to around 50 MW and have a highest single-pixel FRP of 1008 MW. These differences result from the VIIRS I-Band pre-aggregation saturation at the higher FRP AF pixels (Section 2.2; and Schroeder et al., 2014), but fortunately the VIIRS M-Band FRP retrievals are unaffected by such saturation and thus extend to the correct FRP maxima.

6.3. Scan angle impacts

In addition to MODIS' difficulty in detecting low FRP AF pixels (<6 to 8 MW) due to its 1 km^2 nadir pixel area (Fig. 11), Freeborn et al. (2011) also demonstrate that because MODIS' pixel areas are ~10× larger at the scan edge than at nadir, so roughly is the minimum FRP detection limit. VIIRS' pixel aggregation scheme (Section 2.2) results in pixel areas varying much less across the swath (Wolfe et al., 2013), which should make the FRP detection limit also more consistent. Fig. 12 confirms this, where for MODIS the minimum but also the maximum, mean and median FRP strongly increase away from nadir, but where the VIIRS I-Band and M-Band derived FRPs show much more uniformity.

Taking the three VIIRS I-Band aggregation zones in turn, a total of 38%, 24% and 38% of all detected AF pixels were found in these regions respectively; far more uniform than with MODIS - where 77% are located close to the swath centre (within ±32° scan angle) and only 10% at scan angles >45° (and the latter is actually an overestimate because of across-track AF pixel duplication caused by the bow-tie effect; Freeborn et al., 2011). Similar bow-tie effect impacts with VIIRS are absent due to the aforementioned SDR zero filling (Fig. 1a).

6.4. Direct VIIRS to MODIS FRP comparisons

As a last step, we directly compared VIIRS and MODIS FRP outputs with 10-min time difference or less, both on a fire pixel cluster basis (i.e. a group of 1 to 11 spatially adjacent MODIS AF pixels, and the matching VIIRS pixels covering the same geographic area), and on a 1° grid-cell basis. The former required manually matching up individual fires, so was applied to a single day only (10th June 2015), whilst the latter was applied across the entire 13-month study period. Given MODIS' FRP scan angle dependence (Fig. 12), we limited comparisons to a maximum MODIS scan angle of 32°, but no limit was placed on VIIRS since Fig. 12 shows no significant VIIRS scan-angle dependencies.

Fig. 13a shows the per-fire cluster comparison, where the VIIRS I-Band typically underestimates FRP compared to 'close-to-swath-centre' MODIS (slope of linear best fit = 0.19) as a result of I4-Band saturation (Section 2.2). This is the same reason the VIIRS I-Band FRPs of Fig. 11 fail

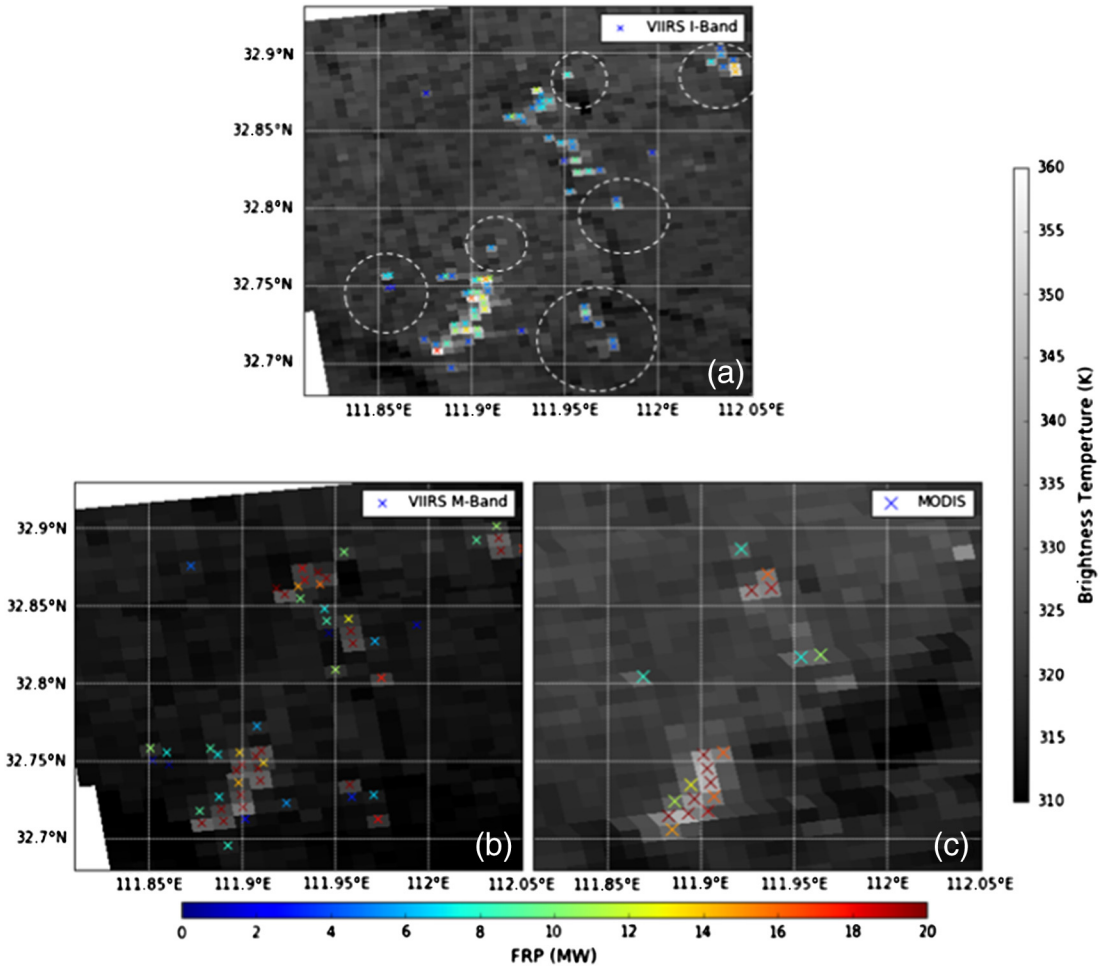

Fig. 9. Active fire (AF) detections made near simultaneously over a 26 km × 26 km region of the study area of Fig. 2 based on different methods and data. Highlighted by the '×' symbols are (a) the VIIRS I-Band AF pixel detections based on the scheme developed herein, superimposed on the source I4-Band MWIR imagery; (b) the VIIRS M-Band pixels containing I-Band detected AF pixels, superimposed on the M13-Band MWIR imagery; and (c) MODIS AF detections, based on the scheme of Giglio et al. (2016). The colour of the crosses depicts the FRP of the detected AF pixel, considered later in Section 6.3. Example active fire pixels detected by our VIIRS I-Band scheme but not by MODIS are circled in (a).

to exceed ~30 MW. VIIRS M-Band FRPs made at the site of the I-Band AF detections (Fig. 13b) show a far better agreement with those from these same MODIS data (slope of linear best fit = 1.01). Those slopes will increase to 0.55 (I-Band) and 1.21 (M-Band) when limiting the data input to those total cluster FRP under 300 MW, indicating the lower impact of I4-Band saturation for smaller fires, as highlighted in Fig. 13a–b.

Fig. 13d and e show, respectively, results of the 1° grid cell based comparisons of VIIRS I-Band FRP's and VIIRS M-Band FRPs (made at the site if the I-Band AF detections) compared to 'close-to-swath-centre' MODIS FRP's. FRP's from VIIRS I-Band and MODIS show a slope increase from 0.19 at the cluster level (Fig. 13a) to 0.64 at the grid-cell level (Fig. 13d). The I-Bands ability to detect many more AF pixels in a grid cell than does MODIS (even close to its swath centre) somewhat counteracts the impact of the I-Band saturation with regard to the grid cells total FRP. However, higher FRP AF pixels will be affected by I-Band saturation, and Fig. 13e shows that when the VIIRS M-Band FRPs measured at the location of the I-Band AF detections are used in place of the I-Band FRP measures themselves, the slope of the linear-best-fit with respect to MODIS increases dramatically (to 1.87). This indicates that nearly half of the study regions' FRP is being emitted by low FRP ("small") fires, undetectable by even 'relatively close-to-swath-centre' MODIS data (i.e. MODIS scan angle ≤32°), a fact also evidenced by the data of Fig.11. Extending the grid-cell comparison to the entire MODIS swath (not shown) increases the slope of the linear-best-fit between the VIIRS M-Band FRPs (assessed at the I-Band-detected AF pixel locations) and MODIS FRPs even more dramatically (to 3.11), because MODIS fails to detect a greater proportion of AF pixels towards the scan edge due to the greatly elevated minimum FRP detection limits away from nadir (shown in Fig. 12). By contrast, Fig. 12 shows that VIIRS AF pixel detection sensitivity is much more constant across the swath due to its unique pixel aggregation scheme.

6.5. Combining VIIRS I- and M-Band FRP measures to optimise FRP retrievals

Though VIIRS I-Band data is clearly extremely useful for detecting low FRP fires, the data of Fig. 13a and d demonstrate that higher FRP fires often saturate the I4-Band, leading to an underestimated FRP compared to simultaneously recorded M-Band data (see Section 2.2). Saturation affecting all pre-aggregation I4-Band measurements is identifiable from the VIIRS SDR Quality Flag data, but that affecting only some pre-aggregation pixels is more difficult to identify (see Appendix B). The VIIRS 750 m spatial resolution M13 data apparently does not suffer saturation effects in our agriculturally-dominated study region, unlike in other areas where much higher FRP fires are more common (e.g. Polivka et al., 2015), and so it can be used for unsaturated FRP retrievals at the location of I-Band detected active fire pixels (as in Figs. 9, 11, 12 and 13). However, where unsaturated I-Band data exist it is better to retrieve FRP from them, because (for the same sub-pixel sized fire) the AF pixel spectral radiance (L_f) is raised more above the background radiance (L_b) in the I-Band than the M-Band, making σ_{FRP} (Eq. (35)) generally much lower for the I-Band FRP than the M-Band FRP. The optimum strategy is thus to combine I-Band and

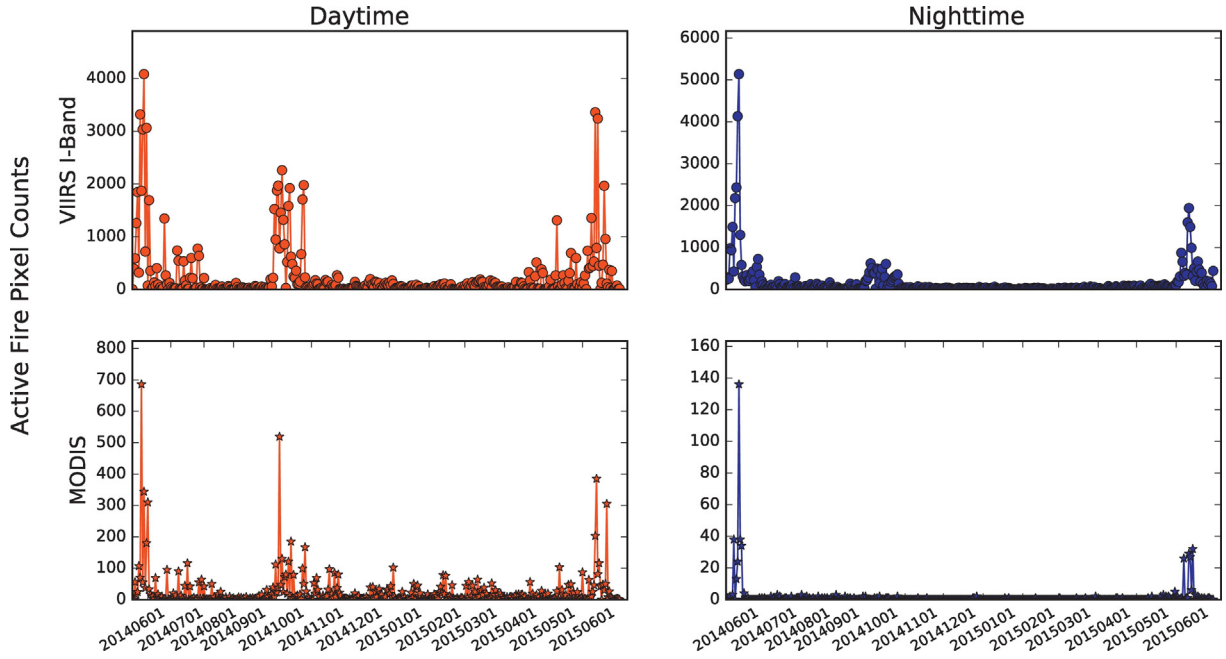

Fig. 10. Daily time-series of AF pixel counts made across the eastern China agricultural region (Fig. 2) between 1st June 2014 and 31st June 2015. Top row shows the daytime and nighttime AF pixel detections made using the VIIRS I-Band scheme developed herein, whereas the bottom row shows those from Aqua MODIS Collection 6 (MYD14). (For interpretation of the references to colour in this figure legend, the reader is referred to the web version of this article.)

M-Band FRP outputs, which we do here to produce a final 'VIIRS-IM' synergy FRP product that selects to record the following FRPs:

(i) For low FRP AF pixels (M-Band FRP ≤ 8 MW), where calculations indicate pre-aggregation I4-Band saturation is almost totally avoided, the algorithm selects whichever of the M-Band and combined I-Band FRPs show lowest FRP uncertainty (according to Eq. (35)). These lowest FRP retrievals, which can extend below 1 MW for the smallest detectable fires, are generally higher for the I-Band than the M-Band, suggesting the likely absence of I4 saturation. This rule selects the FRP output from the VIIRS I-Band data in >90% of cases examined.

(ii) For higher FRP AF pixels (M-Band FRP > 8 MW) whichever I-Band and M-Band FRP is larger is selected for inclusion, because pre-

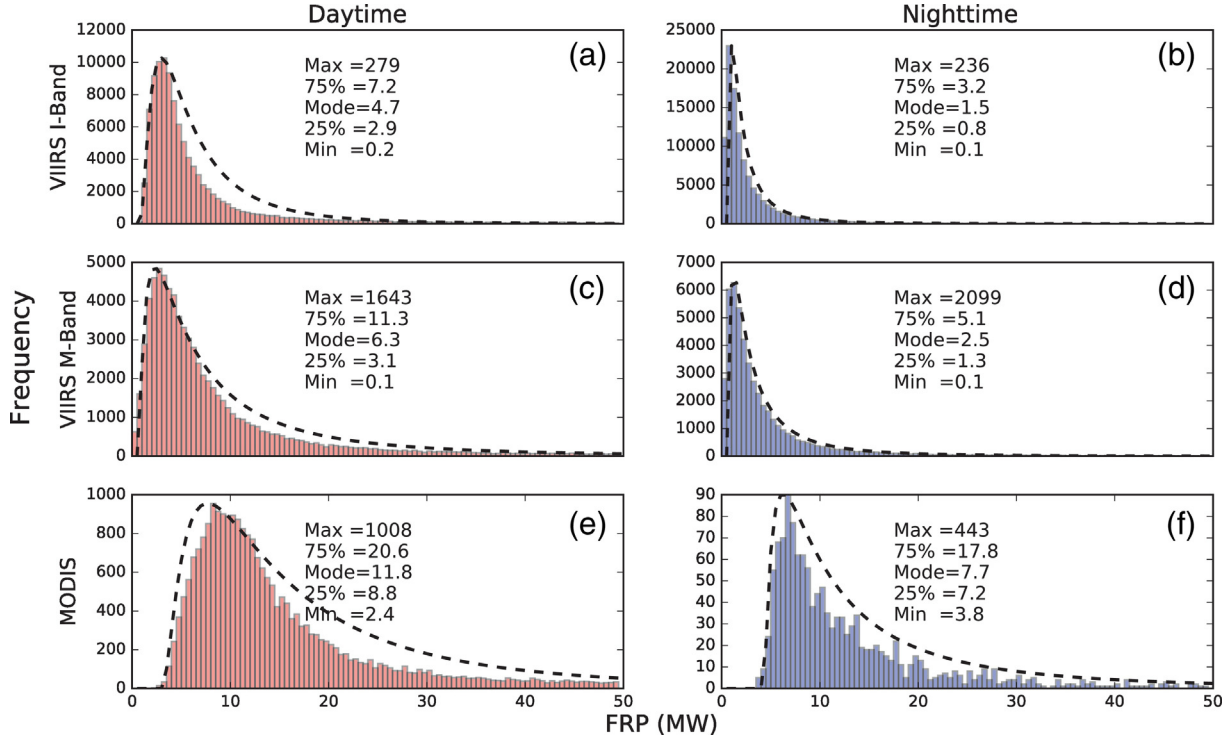

Fig. 11. Frequency distribution of the atmospherically corrected FRP of AF pixels detected over the study region using different data and methods (June 2014–June 2015). AF detections and FRP were derived (a) using the VIIRS I-Band scheme developed herein during the day, and (b) the same scheme but applied at night, (c) from the VIIRS M-Band data recorded at the locations of our I-Band active fire detections by day, and (d) by night, and (e) from MODIS C6 MYD14 by day and (f) by night. All data were atmospherically corrected using MODTRAN-5 as described in the main text, and the dashed lines show log-normal fits to the distribution. The maximum, 75% and 25% percentiles, mode, and minimum of each distribution are also shown.

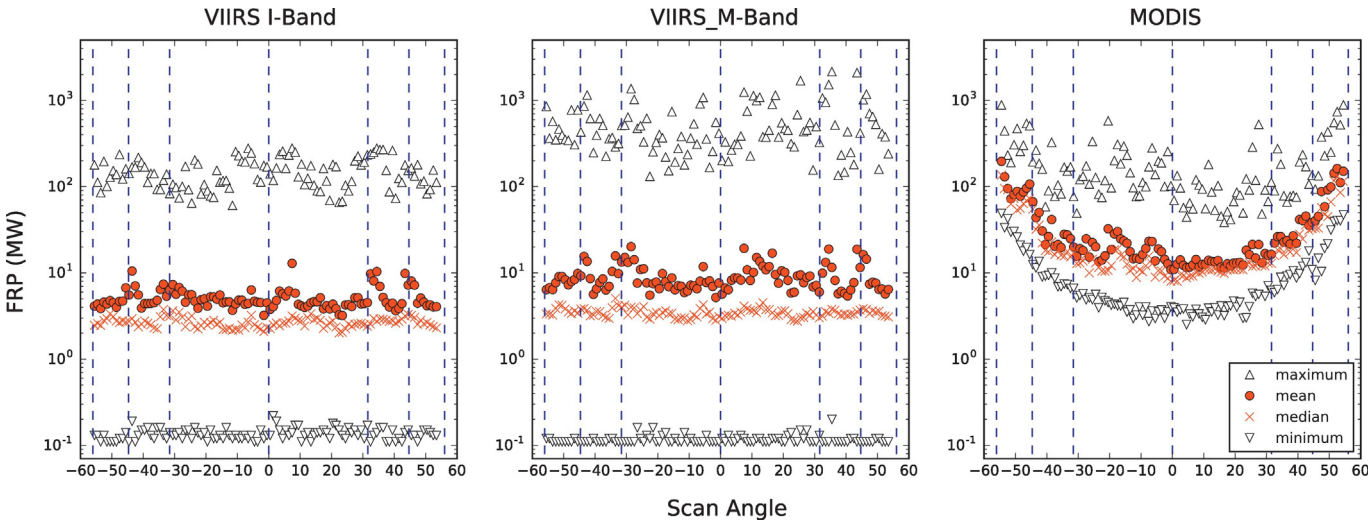

Fig. 12. Variation of maximum, mean, median and minimum per-pixel FRP with scan angle, for the VIIRS I-Band, VIIRS M-Band (calculated using the coincident M-Band radiance for I-Band AF pixels) and MODIS data recorded over our study region (1st June 2014 to 30th June 2015). The blue dashed vertical lines indicate the transition between aggregation zones in VIIRS, and we show them superimposed also on MODIS. The aggregation scheme used by VIIRS to minimise pixel area variations across the swath has very significantly reduced the along-scan variability of these FRP metrics with VIIRS compared to MODIS. (For interpretation of the references to colour in this figure legend, the reader is referred to the web version of this article.)

aggregation I4 saturation will artificially depress the FRP retrievals at certain higher FRP pixels. The clear majority of these AF pixels have their FRP retrieved via the M-Band.

Overall in the 'VIIRS-IM' synergy FRP product developed here, in the 13-month period sampled across the eastern China study area, I-Band-derived FRP contributes 95% of the total FRP in case (i) and M-Band-derived FRP contributes 75% of total FRP in case (ii). Furthermore, in case (ii), the I-Band retrieved FRP's were dominated by FRP's just above the 8 MW limit, because at FRPs much higher than this the I-Band pre-aggregation saturation almost always limits the retrieved FRP to be below the M-Band retrieved FRP.

Across the entire FRP range, the total FRP contributed by small fires (≤8 MW) accounts for around 16% of the total assessed FRP, whereas

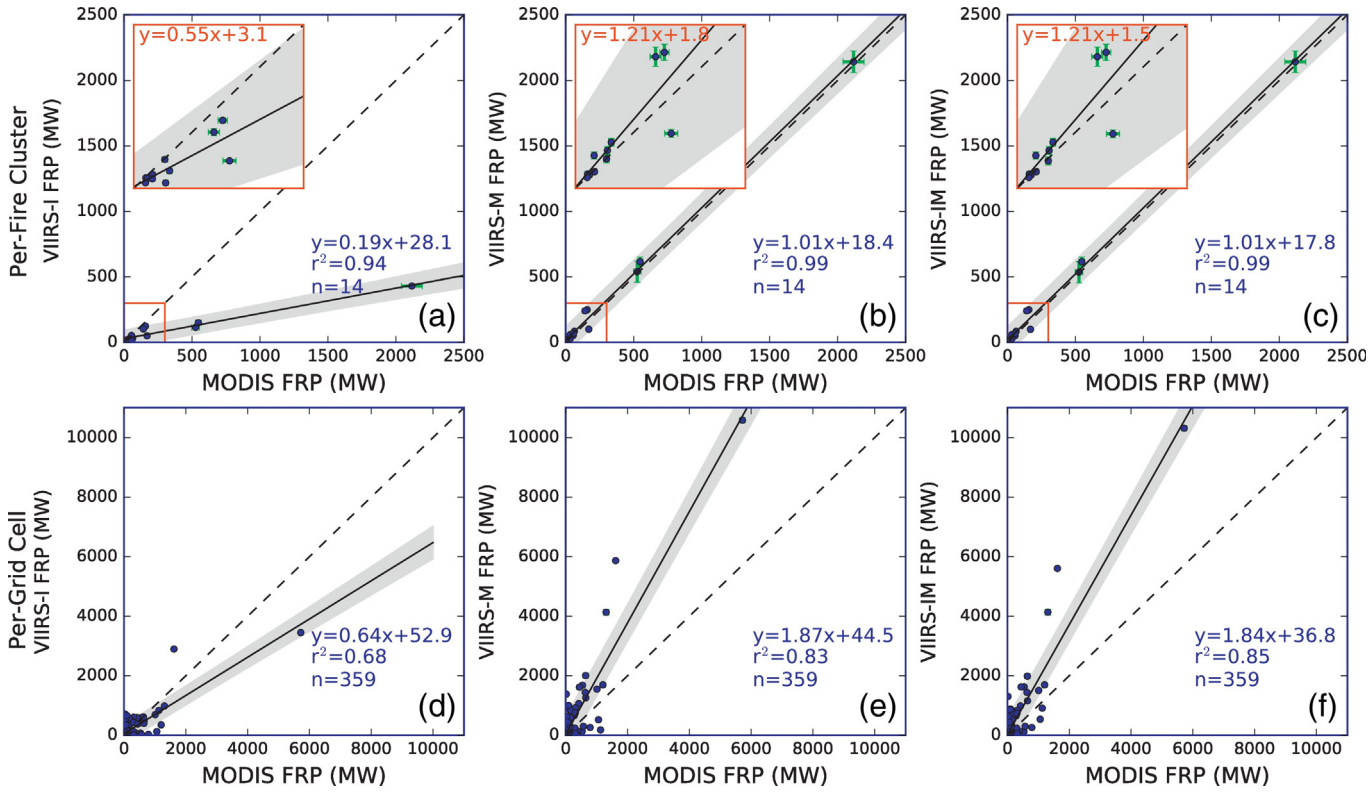

Fig. 13. Direct VIIRS-to-MODIS FRP intercomparisons, conducted using both VIIRS I-Band and M-Band FRP retrievals, and VIIRS-IM 'synergy' FRP product (Section 6.5) at both the scale of individual active fire clusters (a–c), and 1° degree grid cells (d–f). Error bars representing the FRP uncertainty calculated using Eq. (35) are shown in x and y, albeit they are small and difficult to see, especially in d-f. The best fit linear relationships are shown, along with its equation, and the grey shaded area represents the 95% confidence limit on the relationship. The red windows in panels a–c show the highlighted <300 MW data points of main plot with best fit linear relationships and their equations. (For interpretation of the references to colour in this figure legend, the reader is referred to the web version of this article.)

that from larger fires (>8 MW) accounts for the around 84%. As shown in Fig. 13c and f, the slopes of the linear best fits between the VIIRS-IM FRPs and 'close-to-swath centre' MODIS FRPs are similar to those derived with the VIIRS M-Band and MODIS data alone (Fig. 13b and e). Clearly higher FRP AF pixels detected by VIIRS are responsible for the majority of total FRP release, and many of these can in fact also be detected by MODIS when imaged relatively close to the MODIS swath-centre. However, as Fig. 12 indicates, away from the MODIS swath centre the minimum FRP detection limit of MODIS rises dramatically, whereas that for VIIRS does not, meaning that differences between simultaneous VIIRS and MODIS total FRP observations made at the grid cell level increase substantially when more edge-of-swath MODIS data are included in the comparison. Unfortunately for users of MODIS AF data, such edge-of-swath observations are required to be used if daily observations are required.

Fig. 14 compares the spatial pattern of our VIIRS-IM synergy FRP product with that of MODIS FRP data at 0.1° resolution, with all MODIS data now being included rather than just that from close to the swath centre. There is no obvious major difference in the broad spatial distribution, with a large fire-affected area seen bounded by 32–36° N and 114–118° E, and with mostly higher per grid cell FRPs during June than October. This agrees with past suggestions that the central provinces of Shandong, Jiangsu, Anhui and Henan (mainly in the North China Plain) are the source areas of most agricultural fire emissions (Huang et al., 2012; Qin and Xie, 2011; Streets et al., 2003). During June, the most fire-affected areas extend further west and north than in October, including to the west of Henan Province and south of Hebei Province. There are far fewer fires in the Yangtze Plain than in the North China plain, perhaps due to different landscape management practices and increased abilities for agricultural residues to be used in local industries (Liu et al., 2008). Within each grid cell, total FRP is generally higher when assessed using our VIIRS-IM synergy product than when using MODIS, due to VIIRS' greater ability to detect the (very numerous) low FRP fire pixels, and total FRP observed across the study region is larger than that of MODIS by 500% in June 2014, 600% in Oct 2014

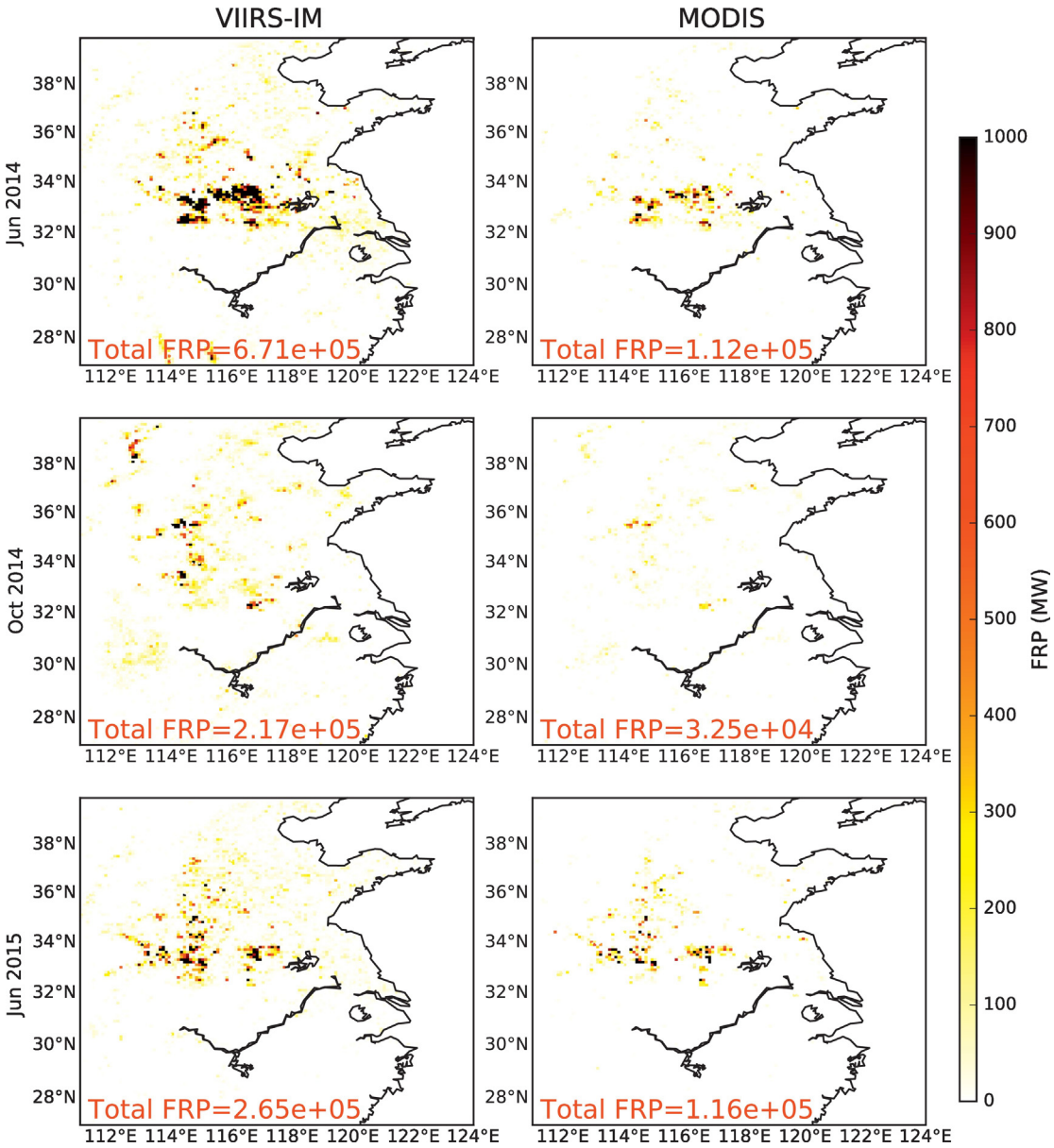

Fig. 14. Spatial distribution and total grid-cell FRP of agricultural fires in eastern China observed during June 2014 (upper row), October 2014 (middle row) and June 2015 (lower row), as assessed using the VIIRS-IM synergy FRP scheme developed here (left column) and MODIS (right column). Total summed regional FRP for each month is also indicated, with VIIRS always significantly higher.

and 100% in June 2015. In the latter case, one particular day (11th June) shows unusually high FRP values, responsible for 62% of the total VIIRS-IM FRP of the whole of June 2015. On this date, the fire-affected area is imaged close to the MODIS swath edge, with large MODIS pixels approaching 10× their area at nadir. Many individual VIIRS AF pixels fall in these large MODIS pixels, and because many are also strongly burning a lot of them trigger MODIS AF detections, even though the MODIS FRP detection limit is significantly raised at near swath edge locations (see Fig. 12). These MODIS AF pixels and their FRP are then replicated along-track due to the MODIS 'bow-tie' effect, which can lead to very significant overestimation of the MODIS-measured. The effect seen on this day therefore contributes very significantly to the total FRP from MODIS for June 2015 being much closer to that from VIIRS-IM than is the case for the other two months, where such burning conditions and sensor viewing geometries were not as fortuitously aligned.

7. Summary and conclusions

We have developed a regional active fire (AF) detection scheme for use with NPP VIIRS, optimising it in this case for the eastern China agricultural region where small (i.e. lower fire radiative power [FRP]) fires dominate due to widespread agricultural residue burning. We have focused primarily on exploitation of 375 m VIIRS I-Band data to detect even very low FRP fires (FRP < 1 MW), and have included detailed procedures to deal with the false alarms that can tend to increase when trying to detect lower FRP fire pixels, and which appear to have been particularly problematic in this area of China during development of the global VIIRS I-Band active fire detection scheme (Schroeder et al., 2014). A small number of AF pixel detections have been validated using pre- and post-fire high spatial resolution imagery, which showed burned areas appearing around the time of the AF detection.

Our VIIRS-based approach shows significant advantages when compared to the simultaneously recorded Collection 6 MODIS MYD14 AF products. The VIIRS approach detects active fires with an FRP-minimum below 0.5 MW, compared to around 6–8 MW for MODIS, and identifies typically 5 to 10× more AF pixels (notwithstanding differences in spatial resolution that mean that sometimes multiple VIIRS AF pixels may be represented by a single MODIS AF pixel). Many studies, including Wooster and Zhang (2004) and Ichoku et al. (2008) have shown that low FRP fires are by far the most common type, indicating that the ability to detect fires below the MODIS FRP detection limit may have a dramatic effect on the total amount of FRP quantified in an area.

It is worth pointing out that combining use of any particular active-fire capable EO data source with an algorithm that includes more liberal thresholds than applied previously does come at the risk of introducing a higher false alarm rate, since a greater range of lower magnitude non-fire phenomena can perhaps exceed the set detection thresholds. This has been countered here via the addition of extra tests, beyond those typically applied in most polar orbiting active fire detection algorithms (for example the spatial filter test), alongside very detailed false alarm screening based on (i) screening out thermal anomalies that are detected in landcover types typically associated with false alarms in this region (i.e. urban areas and manmade structures surrounded by rural landscapes), and (ii) identifying signatures thought largely incompatible with real active fire behaviour (i.e. repeated active fire detections made in the same location, including at times outside of the agricultural burning seasons). The accuracy and representativeness of the ancillary dataset used for the landcover screening is clearly important for the reliability of such approaches, and as further very high spatial resolution data and landcover mapping becomes available to identify such landforms - the accuracy of the approach will improve further. At the present time, it is the case that some urban/industrial areas still fail to be depicted in the current landcover data (Fig. 7c).

Our scheme includes FRP retrieval from the VIIRS M-Band when I-Band data are suspected of being affected by pre-aggregation saturation. Our resulting VIIRS-IM 'synergy' FRP product blends the advantages offered by the VIIRS I-Band sensitivity to small fires with M-Band FRP retrieval over higher FRP fires, and includes appropriate consideration of the waveband and atmospheric transmittance differences between the VIIRS I4 and M13 bands. Over three burning seasons in eastern China, our VIIRS-IM synergy FRP product captures on average 400% more total FRP than does near simultaneous MODIS Collection 6 AF data, even without adjustment for the MODIS 'bow-tie' effect that duplicates MODIS AF pixels towards the swath edge (Freeborn et al., 2011). Our work demonstrates the importance of both VIIRS' ability to detect low FRP fires with the I-Band (see Fig. 11), and its ability to detect active fire pixels with a sensitivity that does not degrade markedly across the swath as does that of MODIS' (see Fig. 12). Our results also prove the key importance of 'small' (i.e. low FRP) fires when quantifying fire emissions in agricultural biomes, but also show the importance of using high quality ancillary data to help mask false alarms. In the most recent implementation of the Schroeder et al. (2014) global 375 m VIIRS active fire product (https://viirsland.gsfc.nasa.gov/Products/FireESDR.html), FRP retrievals for 375 m I-Band pixels are also now made, based on coincident M-Band radiances, and the full data record can be expected soon. We believe our VIIRS-IM Band synergy FRP approach will be highly valuable when applied in other biomass burning regions, particularly those more dominated by low FRP fires, and that working with VIIRS will enable significant improvements in global fire emissions estimation in the coming years.

Acknowledgements

We gratefully thank Lili Wang and her research team for their excellent assistance during fieldwork in eastern China, and Bruce Main for fieldwork preparation and deployment. We thank Wilfrid Schroeder for useful discussions at the start of this work with regard to VIIRS, and gratefully acknowledge the King's China Award and King's Graduate School who funded T. Zhang. NERC Grant's NE/J010502/1 and NE/M017729/1, along with the STFC Newton China Agritech Programme supported aspects of this work. The VIIRS SDR and MODIS data were retrieved from CLASS and Reverb, and are courtesy of the NASA EOSDIS LP DAAC and USGS EROS Centre, South Dakota. Certain map data is copyright of the OpenStreetMap contributors. All data storage and processing was conducted using the UK's JASMIN super-data-cluster system, managed by UK STFC's Centre for Environmental Data Analysis (CEDA). We are grateful to the three anonymous referees for their constructive input.

Appendix A. Variability of atmospheric transmissivity

The uncertainty in atmospheric transmissivity ($\propto_{\tau_{MIR}}$) comes from both the transmission uncertainty due to atmospheric vertical composition apart from water vapour ($\propto_b$), along with the transmission uncertainty associated with the water vapour concentration ($\propto_{H20}$):

$$\propto_{\tau_{MIR}} = \sqrt{\propto_b^2 + \propto_{H2o}^2} \tag{A1}$$

We combined the three equations below, taken from Wooster et al. (2015), to estimate these variables:

$$\propto_b = 10^{-5}\tau_{MIR}\left(710.51117 - 8.37751\theta_v + 0.92238\theta_v^2 - 0.2525\theta_v^3 + 0.00027\theta_v^4\right) \tag{A2}$$

$$\propto_{H20} = \frac{\partial\tau_{MIR}}{\partial U_{H20}} \propto_{U_{H20}} \tag{A3}$$

$$\propto_{U_{H20}} = 0.24287 + 0.11172U_{H20} - 0.00090U_{H20}^2 \tag{A4}$$

Appendix B. FRP underestimation of VIIRS I-Band

Fig. 13c and f (main paper) demonstrate the very significant FRP underestimation that results from use of only the VIIRS I-Band to generate the FRP information, as opposed to both the I-Band and M-Band, and here we discuss the main reasons for these I-Band effects.

A VIIRS I4 pixel has an associated saturation flag set in the VIIRS Quality Flag (QF) data only if all pre-aggregation pixels are themselves saturated. By day, such pixels only account for 3% of the active fire pixel detections made with our I-Band scheme, and by night <1%. However, the summed FRP of these pixels accounts for as high as 9% of the total FRP calculated using the matching VIIRS M-Band pixels, attesting to the significance of dealing with the saturation issue. However, it is also the case that there may be many more cases where saturation only affects some (as opposed to all) the pre-aggregation I4-Band pixels, and these cases are not identified in the QF data (Polivka et al., 2015).

To investigate this, we compared FRP retrievals made from matching I-Band and M-Band pixels. Since each M-Band pixel contains four I-Band pixels, the former might sometimes capture some FRP from I-Band pixels containing fires but which were not detected as such by our I-Band active fire detection algorithm. Therefore, we first selected only those M-Band pixels for which all four constituent I-Band pixels were also identified as containing active fires, but for which no saturation flag was set. We summed the FRP from these I-Band fire pixels and compared them to the matching VIIRS M-Band FRP measure (Fig. A1). For detections made in the VIIRS 'No Aggregation Zone', the linear best fit between the I-Band and M-Band derived FRPs has a slope of 0.69, decreasing to 0.49 for Aggregation Zone 2, and 0.27 for Aggregation Zone 3. The reduction in slope from 'No Aggregation Zone' to 'Aggregation Zone 2' indicates that perhaps 20% ((0.49-0.69)/1) of the FRP underestimation might be due to some (but not all) of the constituent I-Band pixels being saturated before aggregation, a situation that becomes even worse in Aggregation Zone 3 where twelve original I-Band pixels contribute to the I-Band FRP measure to be compared to that from the M-Band (as opposed to the eight I-Band observations in Aggregation Zone 2). However, results for Aggregation Zone 3 can be separated into two groups, whose linear best fits to the matching M-Band FRP data have slopes of 0.1 and 0.84 respectively (likely representing matchups with and without significant I-Band pre-aggregation detector saturation). FRP underestimation due to I-Band pre-aggregation saturation could seemingly therefore be as high as 74% in VIIRS Aggregation Zone 3. Therefore, this comparison shows in Fig. A1 highlights the importance of implement a dual FRP retrieval using both I-Band and M-Band.

References

Cao, C., Xiong, J., Blonski, S., Liu, Q., Uprety, S., Shao, X., ... Weng, F., 2013. Suomi NPP VIIRS sensor data record verification, validation, and long-term performance monitoring. J. Geophys. Res.-Atmos. 118 (20).

Chen, J., Chen, J., Liao, A., Cao, X., Chen, L., Chen, X., He, C., Han, G., Peng, S., Lu, M., Zhang, W., 2015. Global land cover mapping at 30m resolution: a POK-based operational approach. ISPRS J. Photogramm. Remote Sens. 103, 7–27.

Freeborn, P.H., Wooster, M.J., Roberts, G., 2011. Addressing the spatiotemporal sampling design of MODIS to provide estimates of the fire radiative energy emitted from Africa. Remote Sens. Environ. 115, 475–489.

Freeborn, P.H., Cochrane, M.A., Wooster, M.J., 2014. A decade long, multi-scale map comparison of fire regime parameters derived from three publically available satellite-based fire products: a case study in the Central African Republic. Remote Sens. 6 (5), 4061–4089.

Giglio, L., Descloitres, J., Justice, C.O., Kaufman, Y.J., 2003. An enhanced contextual fire detection algorithm for MODIS. Remote Sens. Environ. 87, 273–282.

Giglio, L., Csiszar, I., Justice, C., 2006. Global distribution and seasonality of active fires as observed with the Terra and Aqua Moderate Resolution Imaging Spectroradiometer (MODIS) sensors. J. Geophys. Res. 111, G02016.

Giglio, L., Csiszar, I., Restás, Á., Morisette, J.T., Schroeder, W., Morton, D., Justice, C.O., 2008. Active fire detection and characterization with the advanced spaceborne thermal emission and reflection radiometer (ASTER). Remote Sens. Environ. 112, 3055–3063.

Giglio, L., Randerson, J.T., van der Werf, G.R., Kasibhatla, P.S., Collatz, G.J., Morton, D.C., DeFries, R.S., 2010. Assessing variability and long-term trends in burned area by merging multiple satellite fire products. Biogeosciences 7, 1171–1186.

Giglio, L., Schroeder, W., Justice, C.O., 2016. The collection 6 MODIS active fire detection algorithm and fire products. Remote Sens. Environ. 178, 31–41.

Huang, X., Li, M., Li, J., Song, Y., 2012. A high-resolution emission inventory of crop burning in fields in China based on MODIS thermal anomalies/fire products. Atmos. Environ. 50, 9–15.

Ichoku, C., Martins, J.V., Kaufman, Y.J., Wooster, M.J., Freeborn, P.H., Hao, W.M., Baker, S., Ryan, C.A., Nordgren, B.L., 2008. Laboratory investigation of fire radiative energy and smoke aerosol emissions. J. Geophys. Res.-Atmos. 113, D14S09.

Kaiser, J.W., Heil, A., Andreae, M.O., Benedetti, A., Chubarova, N., Jones, L., Morcrette, J.J., Razinger, M., Schultz, M.G., Suttie, M., van der Werf, G.R., 2012. Biomass burning emissions estimated with a global fire assimilation system based on observed fire radiative power. Biogeosciences 9, 527–554.

Lawrence, B.N., Bennett, V.L., Churchill, J., Juckes, M., Kershaw, P., Pascoe, S., Pepler, S., Pritchard, M., Stephens, A., 2013. Storing and manipulating environmental big data with JASMIN. Big Data, 2013 IEEE International Conference on, pp. 68–75.

Liu, H., Jiang, G.M., Zhuang, H.Y., Wang, K.J., 2008. Distribution, utilization structure and potential of biomass resources in rural China: with special references of crop residues. Renew. Sust. Energ. Rev. 12, 1402–1418.

National Bureau of Statistics of China (NBSC), 2012. China Statistical Yearbook. China Statistics Press, Beijing.

Oudrari, H., McIntire, J., Xiong, X., Butler, J., Ji, Q., Schwarting, T., Lee, S., Efremova, B., 2016. JPSS-1 VIIRS radiometric characterization and calibration based on pre-launch testing. Remote Sens. 8 (1), 41.

Pan, X.L., Kanaya, Y., Wang, Z.F., Komazaki, Y., Taketani, F., Akimoto, H., Pochanart, P., 2013. Variations of carbonaceous aerosols from open crop residue burning with transport and its implication to estimate their lifetimes. Atmos. Environ. 74, 301–310.

Piper, M., Bahr, T., 2015. A rapid cloud mask algorithm for Suomi NPP VIIRS imagery EDRs. Int. Arch. Photogramm. Remote. Sens. Spat. Inf. Sci. 40 (7), 237.

Polivka, T.N., Hyer, E.J., Wang, J., Peterson, D., 2015. First global analysis of saturation artifacts in the VIIRS infrared channels and the effects of sample aggregation. IEEE Geosci. Remote Sens. Lett. 12, 1262–1266.

Qin, Y., Xie, S.D., 2011. Historical estimation of carbonaceous aerosol emissions from biomass open burning in China for the period 1990–2005. Environ. Pollut. 159, 3316–3323.

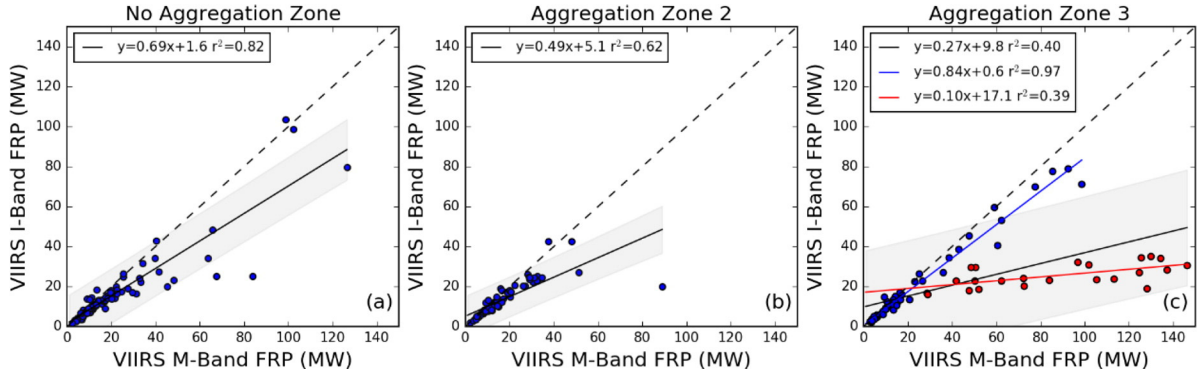

Fig. A1. Comparison of FRP values derive from matching VIIRS I-Band and M-Band observations of active fire pixels detected in the three VIIRS aggregation zones. Linear best fits and the 1:1 line are also shown. In Aggregation Zone 3 two different patterns are seen and linear best fits are applied to each. These likely represent data where pre-aggregation zone I-Band saturation does not occur or is minimal (slope of 0.84) and where it does (slope of 0.1).

Qu, L., Zhang, T., Lu, W., 2014. Assessing the potential of crop residue recycling in China and technology options based on a bottom-up model. Front. Environ. Sci. Eng. 8, 570–579.
Randerson, J., Chen, Y., Werf, G., Rogers, B., Morton, D., 2012. Global burned area and biomass burning emissions from small fires. J. Geophys. Res. Biogeosci. 2005–2012, 117.
Roberts, G.J., Wooster, M.J., 2008. Fire detection and fire characterization over Africa using Meteosat SEVIRI. IEEE Trans. Geosci. Remote Sens. 46, 1200–1218.
Roberts, G., Wooster, M.J., Perry, G.L., Drake, N., Rebelo, L.M., Dipotso, F., 2005. Retrieval of biomass combustion rates and totals from fire radiative power observations: application to southern Africa using geostationary SEVIRI imagery. J. Geophys. Res.-Atmos. 110 (D21).
Robinson, J.M., 1991. Fire from space: global fire evaluation using infrared remote sensing. Int. J. Remote Sens. 12 (1), 3–24.
Roy, D.P., Frost, P.G.H., Justice, C.O., Landmann, T., Le Roux, J.L., Gumbo, K., Makungwa, S., Dunham, K., Du Toit, R., Mhwandagara, K., Zacarias, A., Tacheba, B., Dube, O.P., Pereira, J.M.C., Mushove, P., Morisette, J.T., Santhana Vannan, S.K., Davies, D., 2005. The Southern Africa Fire Network (SAFNet) regional burned-area product-validation protocol. Int. J. Remote Sens. 26, 4265–4292.
Roy, D.P., Ju, J., Lewis, P., Schaaf, C., Gao, F., Hansen, M., Lindquist, E., 2008. Multi-temporal MODIS–Landsat data fusion for relative radiometric normalization, gap filling, and prediction of Landsat data. Remote Sens. Environ. 112, 3112–3130.
Schroeder, W., Oliva, P., Giglio, L., Csiszar, I.A., 2014. The New VIIRS 375 m active fire detection data product: algorithm description and initial assessment. Remote Sens. Environ. 143, 85–96.
Streets, D., Yarber, K., Woo, J.-H., Carmichael, G., 2003. Biomass burning in Asia: annual and seasonal estimates and atmospheric emissions. Glob. Biogeochem. Cycles 17.
Wolfe, R.E., Lin, G., Nishihama, M., Tewari, K.P., Tilton, J.C., Isaacman, A.R., 2013. Suomi NPP VIIRS prelaunch and on-orbit geometric calibration and characterization. J. Geophys. Res.-Atmos. 118, 11,508–511,521.
Wooster, M.J., Zhang, Y.H., 2004. Boreal forest fires burn less intensely in Russia than in North America. Geophys. Res. Lett. 31 (20).
Wooster, M.J., Zhukov, B., Oertel, D., 2003. Fire radiative energy for quantitative study of biomass burning: derivation from the BIRD experimental satellite and comparison to MODIS fire products. Remote Sens. Environ. 86, 83–107.
Wooster, M.J., Roberts, G., Perry, G.L.W., Kaufman, Y.J., 2005. Retrieval of biomass combustion rates and totals from fire radiative power observations: FRP derivation and calibration relationships between biomass consumption and fire radiative energy release. J. Geophys. Res.-Atmos. 110, D24311.
Wooster, M., Xu, W., Nightingale, T., 2012. Sentinel-3 SLSTR active fire detection and FRP product: pre-launch algorithm development and performance evaluation using MODIS and ASTER datasets. Remote Sens. Environ. 120, 236–254.
Wooster, M.J., Roberts, G., Freeborn, P.H., Xu, W., Govaerts, Y., Beeby, R., He, J., Lattanzio, A., Fisher, D., Mullen, R., 2015. LSA SAF Meteosat FRP products – part 1: algorithms, product contents, and analysis. Atmos. Chem. Phys. 15, 13217–13239.
Yan, X., Ohara, T., Akimoto, H., 2006. Bottom-up estimate of biomass burning in mainland China. Atmos. Environ. 40, 5262–5273.
Zhukov, B., Oertel, D., 2001. Hot Spot Detection and Analysis Algorithm for the BIRD Mission. Algorithm Theoretical Basic Document, DLRBerlin.
Zhukov, B., Lorenz, E., Oertel, D., Wooster, M., Roberts, G., 2006. Spaceborne detection and characterization of fires during the bi-spectral infrared detection (BIRD) experimental small satellite mission (2001–2004). Remote Sens. Environ. 100 (1), 29–51.